



POLITECNICO
MILANO 1863

SCUOLA DI INGEGNERIA INDUSTRIALE
E DELL'INFORMAZIONE

A reduced model for the flow in the human nose

TESI DI LAUREA MAGISTRALE IN
AERONAUTICAL ENGINEERING - INGEGNERIA AERONAUTICA

Author: **Angelo Raimondo Favero**

Student ID: 992655

Advisor: Prof. Maurizio Quadrio

Co-advisor: Dott. Emanuele Gallorini

Academic Year: 2023-24

Abstract

This work presents a reduced model for the computational study of the airflow inside the human nose. The method extends the linear Hele-Shaw approximation to non-planar channels, and uses a variable porosity to represent the complex nasal anatomy. The objective is to obtain results useful to medical experts in diagnosing patients with nasal obstruction and discomfort in nasal respiration. The method is preliminarily applied to the simple geometry of a straight cylinder to verify its correctness. Then, the results obtained for a specific patient are compared with those from a direct numerical simulation (DNS), conducted with the lowest possible pressure drop imposed in the throat to comply with linearity: the most significant features of the flow are well captured. Thanks to the minimal computational cost of the approach, in this thesis a large number of cases can be studied together, taking advantage of an existing database of patients with properly compiled labels. The findings demonstrate the potential of this method, as general patterns concerning the different pathological conditions are observed in the solutions. Although the method still contains aspects that are being improved, for the first time a large-scale multi-patient study could be carried out, paving the way for a revolutionary step change in the way nasal breathing difficulties are assessed.

Keywords: Nasal airflow, Hele-Shaw, Computational Fluid Dynamics

Abstract in lingua italiana

Questo lavoro presenta un modello ridotto per lo studio computazionale del flusso d'aria all'interno del naso umano. Il metodo estende l'approssimazione lineare di Hele-Shaw ai canali non planari e utilizza una porosità variabile per rappresentare la complessa anatomia nasale. L'obiettivo è ottenere risultati utili ai medici nella diagnosi di pazienti con ostruzione nasale e difficoltà nella respirazione nasale. Il metodo viene preliminarmente applicato alla geometria semplice di un cilindro rettilineo per verificarne la correttezza. Quindi, i risultati ottenuti per un paziente specifico vengono confrontati con quelli di una simulazione numerica diretta (DNS), condotta con la minima differenza di pressione possibile imposta nella gola per rispettare la linearità: le caratteristiche più significative del flusso sono ben catturate. Grazie al costo computazionale minimo dell'approccio, in questa tesi è possibile studiare insieme un gran numero di casi, sfruttando un database esistente di pazienti con etichette adeguatamente rispettate. I risultati dimostrano il potenziale di questo metodo, poiché nelle soluzioni si osservano modelli generali riguardanti le diverse condizioni patologiche. Sebbene il metodo contenga ancora aspetti in fase di miglioramento, per la prima volta è possibile condurre uno studio multipaziente su larga scala, aprendo la strada a un cambio di passo rivoluzionario nel modo in cui vengono valutate le difficoltà respiratorie nasali.

Parole chiave: Fluidodinamica nasale, Hele-Shaw, Fluidodinamica computazionale

Contents

Abstract	i
Abstract in lingua italiana	iii
Contents	v
1 Introduction	1
1.1 Importance of the nose flow	1
1.2 Technique and objectives	1
1.3 Structure of the work	2
2 Preliminary concepts and state of the art	3
2.1 Nose Anatomy and Physiology	3
2.1.1 Pathologies	5
2.2 State of the art	6
2.3 Computed tomography	9
2.4 NRRD	10
3 Code implementation and description	13
3.1 Governing Equations	13
3.1.1 Energy dissipation	15
3.2 Hele-Shaw model	15
3.3 Airway geometry and bounding box	17
3.4 Definition of the airways boundary	19
3.5 Hydraulic conductivity	22
3.6 Pressure field	26
3.6.1 Initial Conditions	26
3.6.2 Numerical solution	26
3.7 Velocity and Energy dissipation rate	28

3.8	Flow of air in the nostrils and the throat	29
3.9	Temperature	30
3.9.1	Initial Conditions	30
3.9.2	Thermal Conductivity	30
3.9.3	Numerical Solution	31
3.10	Heat transfer and temperature in the throat	32
3.11	Representation of the results	32
4	Tests and preliminary results	35
4.1	Test on simple geometry	35
4.2	Comparison with DNS	39
4.3	A preliminary multipatient study	45
4.3.1	Effects of radiodensity threshold	45
4.3.2	Correlation between pathologies and results	49
5	Conclusions	55
6	Bibliography	57
A	Code execution on the database	63
A.1	Pathologies' labels	63
A.2	Procedure for the CFD simulation on all the patients	64
	List of Figures	69
	List of Tables	71
	Acknowledgements	73

1 | Introduction

1.1. Importance of the nose flow

The problem of airflow inside the nose is very relevant today. A healthy respiration through the nasal cavity is crucial for a correct respiration process also in the lower airways. Surgeries performed in the nasal airways (e.g., septoplasty, turbinate resection) can be complicated and have a relatively low success rate [1, 2], with patients sometimes presenting new symptoms (e.g. empty nose syndrome)[3]. This thesis is part of the OpenNOSE project, a collaborative effort between the Otolaryngology Department of Milan A.O. San Paolo and the Department of Aerospace Sciences and Technologies at Politecnico di Milano.

The project's objective is to develop a robust and versatile open-source diagnostic methodology. This methodology integrates engineering approaches, specifically Computational (CFD) and Experimental Fluid Dynamics, with medical challenges such as nasal surgery. The goal is to support healthcare professionals in diagnosing and treating patients with pathological conditions that negatively impact their quality of life.

The main objectives of past thesis projects and research work in this context include: the creation of the 3D model [4], the definition of a workflow for the computations [5], the use of more resolved methods such as LES [6] and DNS [7] to compute the flow more accurately and validate results from simpler models, optimization through the use of the adjoint solution [8], and more recently, the implementation of machine learning in the workflow [9].

1.2. Technique and objectives

In this work the tool used is the CFD program **tp3d** written by Professor Paolo Luchini in the Compiler and Programming Language (CPL) [10]. This program computes the airflow within the internal geometry of real noses, with a reduced model, starting from computed tomography (CT) scans and obtaining results on relevant physical quantities inside the nasal cavity extremely fast. For each patient the simulation is carried out in a

few seconds.

The purpose of using such a fast code is to develop a tool that surgeons can utilize in real-time for diagnosis and surgical planning. As this is the first time the code is being described, a significant portion of the thesis will focus on explaining its functionality and testing its results. Another objective is to create an automated process for solving the problem across all cases, generating results quickly, and identifying general correlations between CFD results and anatomical pathologies. Pathological conditions were identified by a team of Ear, Nose, and Throat (ENT) medical experts who diagnosed each patient.

1.3. Structure of the work

- **Preliminary concepts and state of the art:** Introduction to the nose anatomy, review of the literature on computational and experimental methods used to assess nasal flow, followed by some basic concepts necessary to perform the work.
- **Code implementation and description:** An explication of the code and its functionalities, accompanied by the underlying mathematics.
- **Tests and preliminary results:** First the code is tested on the geometry of a straight cylinder. Then is studied the effect of the radiodensity threshold imposed and the effects of the pathologies on the results for all the patients.
- **Conclusions:** Summarizes key findings, discuss the limitations and the possible improvements.

2 | Preliminary concepts and state of the art

2.1. Nose Anatomy and Physiology

To better understand the physical problem, it is important to have a general idea of the architecture of the nasal cavity, focusing on the features that most influence the flow of air. For a more detailed analysis of the relationship between anatomy and flow, the reader can refer to [11], [12], [13], [14], and [15].

The nasal cavity plays a crucial role in respiratory function, not only facilitating breathing but also filtering and humidifying the inhaled air. Structurally, it comprises the nasal bones, turbinates, and mucosa, each contributing to its functionality.

The external nose features a triangular pyramid shape, centrally located on the face between the forehead and the upper lip. It comprises a posterior surface in contact with the frontal bone, two triangular lateral surfaces, and a triangular inferior surface. This inferior surface is defined by two ellipsoidal openings directed downwards, known as nostrils, each approximately one centimeter in diameter. The posterior surface corresponds to the bone structure, specifically the piriform aperture. The lateral surfaces include a fixed upper portion at the nasal bone and a lower, mobile portion bounded by the nose's elastic cartilages [8].

The nasal cavity (Fig. 2.1 [16]), enveloping the nostrils, extends as a dual chamber, each measuring approximately 5 cm in height and 10 cm in length, constituting a total surface area of around 150 cm² and a volume of about 15 ml. This structure is characterized by its narrowest section, the nasal valve, located 1.5 cm from the nostril, which significantly contributes to respiratory airflow resistance, accounting for about 50% of the total from nostril to alveoli.

The nasal cavity is divided in two by the nasal septum, a thin wall of bone and cartilage that extends from the nasal bridge at the top of the nose down to the floor of the nasal

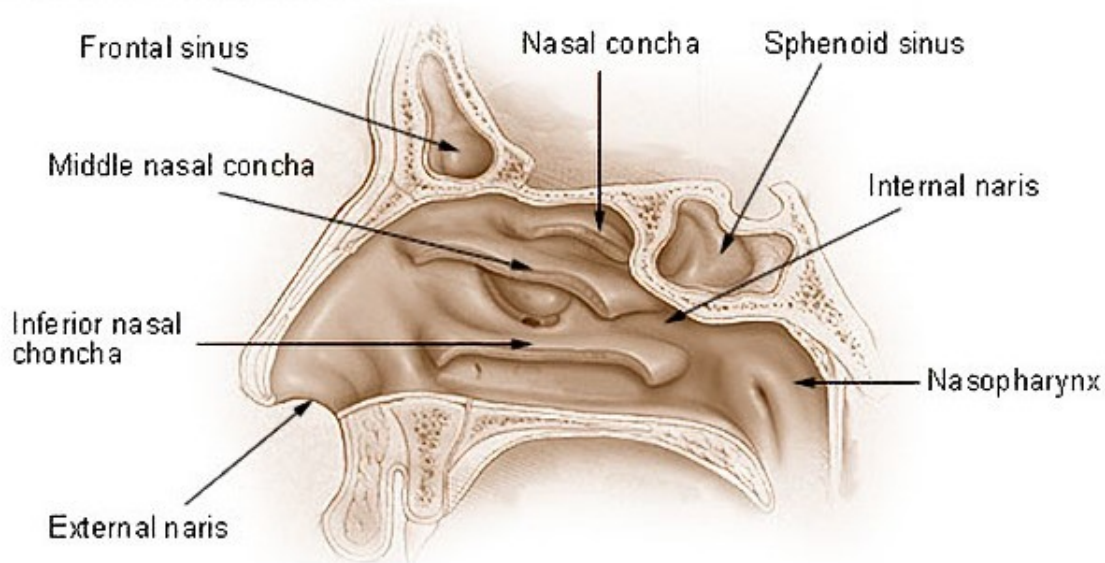


Figure 2.1: Nasal cavity anatomy

cavity. The front portion of the septum is made of cartilage, while the back portion consists of bone. The primary function of the nasal septum is to support the nose, regulate airflow, and help humidify the air breathed by directing it into the nasal passages.

The nasal cavities, bordered by the septal and lateral walls, are further divided by the presence of the inferior, middle, and superior turbinates. The turbinates are thin, plicated, membrane-covered bony or cartilaginous plates on the walls of the nasal chambers. They play a fundamental role in maintaining the cavity's shape, efficiently humidifying, and regulating the temperature of the inspired air.

The inferior turbinate is the largest among the three pairs of turbinates, spanning the full length of the lateral nasal wall, adjacent to the nasal floor. This structure features a lateral vascular cushion that warms and humidifies the air flowing through the nose. The middle turbinate is situated next to the nasal septum, above the inferior turbinate and behind the maxillary sinus. It is particularly important in the process of olfaction and in protecting the sinuses' openings. The superior turbinate is the smallest one and resides above and behind the middle turbinate. It less affects airflow into the cavity, as most air is directed towards the floor of the nasal cavity.

Beneath and lateral to each turbinate lies the *meatus*, a passage that facilitates drainage and airflow. The complexity of this anatomy, particularly the ostiomeatal complex within the middle meatus, is critical in understanding the pathophysiology of sinus diseases.

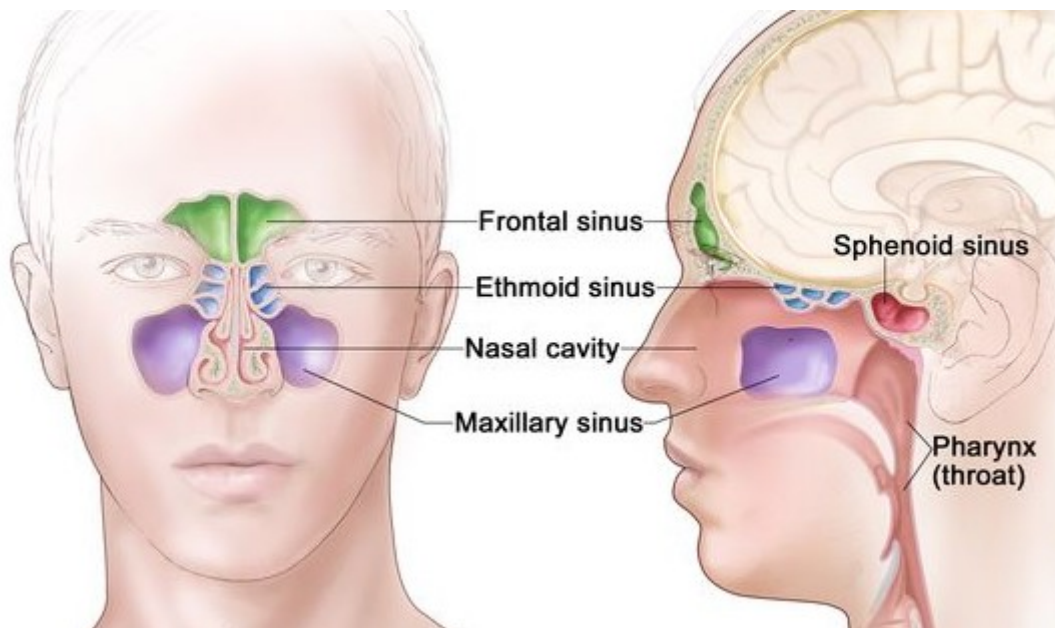


Figure 2.2: Paranasal sinuses

An important part of the upper airway is represented by the paranasal sinuses (Fig. 2.2 [17]). Since the sinuses are connected to the airway through very narrow passages called *ostia*, the air inside them is almost static. Nevertheless, these sinuses are an integral component of the nasal cavity's anatomy and comprise the maxillary, sphenoid, frontal, and ethmoid sinuses.

2.1.1. Pathologies

Pathological conditions can compromise normal nasal respiration. A goal of this work is to study their effect on numerical results. Below is a list with a short description of each pathology considered in this study, including causes, symptoms [18], and visualizations on a CT scan (Fig. 2.3):

- Turbinates pathologies: List of conditions that can affect the turbinates
 - Turbinate hypertrophy: The condition refers to an enlargement of one of the turbinates. This swelling causes obstruction of the nasal cavities: some associated complaints include stuffy nose, runny nose, repeated sneezing, hyposmia, epistaxis and, in the most serious and prolonged cases, sinusitis, pharyngitis, otitis, sleep apnea and nasal polyps. The possible hypertrophies studied are the ones of the middle or inferior turbinates, since the superior turbinate does not affect the flow much.

- *Concha bullosa*: It is a developmental anomaly of the middle turbinate, instead of being a flat bone that delimits the middle *meatus*, it assumes a globular shape and blocks the *meatus*, causing nasal respiratory obstruction, abundant serous rhinorrhea, sneezing and tearing.
- Paradox Curve: It is an anomaly in the development of the middle turbinate: instead of having a slight curvature towards the middle meatus, i.e. the area in which the paranasal sinuses open, favoring the passage of inspired air, it takes on an opposite curvature, towards the nasal septum thus producing nasal respiratory obstruction, purulent nasal discharge, mucus running down the nose into the throat, reduced or lost sense of smell, swelling of the cheek or around the eyes and headache.
- Septal Deviation: This condition appears when the nasal septum is crooked and displaced towards one of the two sides of the nasal cavity, making one of the two passages smaller than the other and causing a pathological nasal respiratory obstruction. Other associated disorders include rhinitis, recurrent nasal discharge, headache, repeated sneezing, pharyngitis and, in the most serious cases, disorders associated with the lower airways (*pharigolaryngo bronchitis*) or the paranasal sinuses (*sinusitis*) or even in the ear (*otitis*). Such a disorder is very frequent in the adult population.

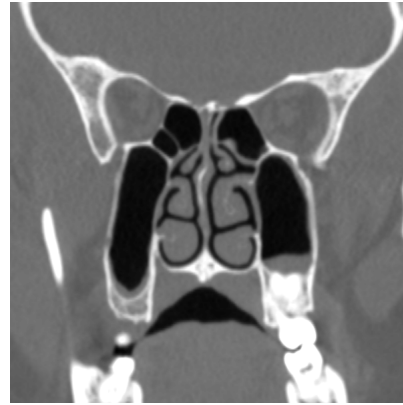
2.2. State of the art

The success rate of surgeries performed on patients with nasal obstruction and related pathologies is relatively low, plus it can happen that patients present new problems related to breathing after the surgery is performed (e.g. empty nose syndrome [3]). For these reasons a coupling between experimental and computational evaluation of the airway, can be crucial to support surgeons in decision making before operations. The studies on the flow of air inside the nasal cavity are relatively recent, the methods applied for this purpose are both *in vivo* and *in vitro*. Particular attention will be given to methods implying the use of Computational Fluid Dynamics. By employing CFD, it is possible to visualize airflow patterns, identify regions of high resistance, and evaluate the effects of surgical modifications, thereby enhancing the understanding of nasal physiology and improving treatment strategies for nasal obstruction and other related conditions.

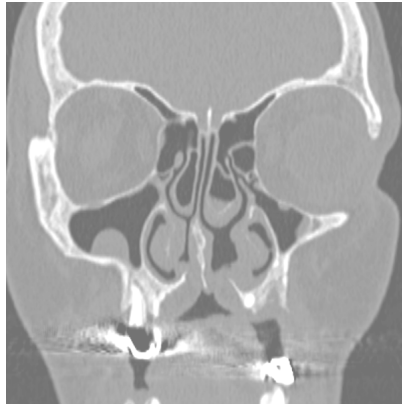
A common parameter measured to characterize the flow inside the nose is the nasal resistance. It is a quantity defined as the ratio of the pressure gradient inside the nasal cavity and the volumetric flow rate of air $R_N = \Delta P/Q$ [19]. The most common method to mea-



(a) Patient 0022: Septal deviation to the left



(b) Patient 0010: Hypertrophy of both inferior and middle Turbinates



(c) Patient 0036: *Concha bullosa* on both sides



(d) Patient 0131: Paradox curve on the right turbinate

Figure 2.3: Pathological situations visualized on a coronal section of the CT

sure this quantity experimentally is anterior rhinomanometry [20], which is a non-invasive medical test that can be easily performed by doctors to evaluate nose obstructions. This test is useful because knowing the nasal resistance can give insights on the airflow, but it does not give nearly as much information as a CFD simulation. In the work by Osman et al. [21], is shown that there is a large discrepancy between the results obtained experimentally with anterior rhinomanometry and the ones from a CFD simulation, with the latter ones underestimating the nasal resistance with respect to anterior rhinomanometry. A possible interpretation is that the resistance measured with rhinomanometry is actually different from the theoretical definition. The causes behind this effect are also studied in a recent master thesis work on the subject [22].

To obtain flow visualization inside the cavity, the most common method used in the field is Particle Image Velocimetry. PIV is the proposed method in [12] and [23] as an

experimental comparison for the computational results obtained. In the context of the OpenNOSE project, using PIV, in [24] is proposed a benchmark for the validation of different numerical approaches to upper airway flow.

Computational Fluid Dynamics (CFD) has emerged as a powerful tool for the study of nasal airflow. This approach enables the simulation and analysis of the impact of various factors on overall respiratory function. CFD simulations can be performed under steady or unsteady conditions, or with a succession of steady-state ones. It is important to understand how much relevant information is lost when considering a steady simulation instead of an unsteady one. Considering the flow in a nasal cavity during a complete respiration cycle with a Reynolds number $Re > 1500$, it has been shown that the differences between the solutions of the steady and unsteady flow fields can be neglected, except for the transition from the inspiration to expiration phase [25]. In this case, the Reynolds number is defined considering the hydraulic diameter at the nostrils' inlet. On the other hand, even if the flow in the nasal cavity is primarily laminar, high inspiration rates can produce instabilities [12]. Instantaneous velocity measurements show regular shedding of structures and unsteadiness of flow, especially in the upper and anterior cavity regions. These phenomena are not seen under steady conditions, and it has been demonstrated that also using RANS to model turbulence would be physically ill-founded.

Using a Large Eddy Simulation (LES) to compute the flow in the airways [26], significant differences in results can be achieved compared to a Reynolds-Averaged Navier-Stokes (RANS) model. The flow is generally unsteady and fully turbulent only in specific parts of the computational domain. For this reason, LES improves the understanding of the spatio-temporal details of the flow that are completely lost in a RANS simulation. Nevertheless, for the purpose of clinical analysis, results with sufficient accuracy can be obtained with lower resolution models, larger time steps, and without turbulence modeling [27]. These results underline the need to study large population samples to account for variations among different patients. In general, the flow inside the nasal cavity cannot be completely described using steady simulations. More resolved methods make it possible to study the particular features of the flow. However, it has been demonstrated that results from computationally less expensive methods are valuable for understanding the most general characteristics of the flow, which are often the ones needed by healthcare providers. This consideration is crucial for highlighting the importance of this thesis work, which aims to find useful results on a large database of patients and to link these results with health conditions, using a simple, steady, and fast computational method.

Exploiting fluid mechanics to find correlations with nasal pathologies has proven to be successful [23], with fluid dynamics results aligning with patient subjective evaluations

and medical expert diagnoses. However, the methods used are still limited in terms of applicability. An important step forward is to develop user-friendly programs that can be used directly by doctors to perform real-time diagnoses.

Extracting the airways geometry from a CT scan, is common practice for the realization of CFD [28]. Normally it is necessary to segment it to create a 3D mesh for performing CFD or to create models for experiments. It will be seen that in the method proposed this passage is not needed.

It is common that the database considered in many works is only composed of few patients [29], [27], [28], each one with a pathology that forms a nasal obstruction of some kind, making it impossible to make general considerations on the results obtained. In this thesis work, the available database is much larger. Additionally all the patients in the database have been diagnosed by ENT experts and it will be possible to observe a pattern in the results of patients with similar health conditions. Another important factor that determines different airflows, are anatomical differences [29]. Different internal geometrical parameters of the airway (such as total area, total volume, hydraulic diameter of the nostril and area of specific sections), have a relevant influence on the airflow.

2.3. Computed tomography

Since a relevant part of the work is related with concepts regarding tomographies, it is considered important to make an introduction on the technique. Computed tomography (CT) is a medical imaging technique that operates using an X-ray generator rotating around an object, together with computer processing, to create detailed cross-sectional images of the body. These images can be used by healthcare professionals to visualize the internal structure of the human body. CT relies on the different capability of the various bodily structures to absorb X-ray radiation. The information is then stored in three-dimensional units called voxels, that are displayed in a grey scale, based on the radiodensity, where white is associated to the most attenuating parts (e.g. bones) and black to least attenuating ones (e.g air). To give a quantitative measurement of the radiodensity of the different tissues Hounsfield units (HU) are used . The Hounsfield scale is a linear transformation of the original linear attenuation coefficient measurement into one referred to the radiodensity of distilled water and air at standard pressure and temperature. Considering a voxel with linear attenuation coefficient μ_x , the corresponding HU value is:

$$HU = \frac{\mu_x - \mu_{water}}{\mu_{water} - \mu_{air}} * 1000 \quad (2.1)$$

Where μ_{water} and μ_{air} are the attenuation coefficients of distilled water and standard air respectively, in Hounsfield units water as an attenuation of 0 HU, while air of -1000 HU. Bones can have values that go from 700 to around 3000 HU.

Changing the radiodensity threshold chosen for extracting the geometry affects the CFD results significantly [30]. Performing a series of CFD computations on the geometry extracted from the same patient, changing the HU threshold to identify the contour of the airway, the numerical results can change a lot, especially for some quantities (e.g flow rate, nasal resistance), while it is less relevant for some other features (e.g. intranasal flow distribution, surface area) [31]. Together with this effect, the threshold chosen can determine whether the airway is entirely extracted correctly. In this thesis will be shown the radiodensity threshold chosen affects also the definition of the interface the solid geometry and air. A study that analyzes the differences between a first order interpolation of the elements on the boundary and the use of a correction, will be performed.

Before beginning with the description of the code, it is important to introduce the reference system that is going to be used. In Fig. 2.4, the reference frame considered is shown in comparison with the anatomic reference system. In this frame, the x -axis is perpendicular to the sagittal plane, the y -axis is perpendicular to the coronal plane, and the z -axis is oriented upwards with respect to the head, perpendicular to the transverse plane.



Figure 2.4: Reference frame and anatomical body planes.

2.4. NRRD

The data collected during the computed tomography can be stored in a Near Raw Raster Data (NRRD) file [32]. NRRD is a file format for the representation and processing of n-dimensional (in this case, 3-dimensional) raster data. Raster graphics represent images as regular grids of values; in the case of a volume, these values are called voxels. Field

specifications for NRRD files are reported in the header, which appears as shown in (2.1).

Listing 2.1: NRRD Header Example Patient (0069)

```
NRRD0004
# Complete NRRD file format specification at:
# http://teem.sourceforge.net/nrrd/format.html
type: int
dimension: 3
space: left-posterior-superior
sizes: 512 512 255
space directions: (0.3398439999,0,0) (0,0.3398439999,0) (0,0,0.625)
kinds: domain domain domain
endian: little
encoding: gzip
space origin: (-86.29999999, -137.3999999, -91.24999999)
```

- **type:** Identifies the type of data within the array. **tp3d** is able to read both signed 2-byte integers (*short*) and signed 4-byte integers (*int*).
- **dimension:** Gives the dimension of the array
- **space:** Specifies the coordinate space of the data array, with the program exclusively supporting the Left-Anterior-Superior (LAS) orientation. The reference frame considered for all the patients is the one shown in Fig. 2.4([33],[34]).
- **sizes:** A vector detailing the count of samples along each spatial direction.
- **space directions:** Describes the positional displacement resulting from a unit increment in each array coordinate, effectively representing the voxel dimensions. If necessary, the program changes the reference frame orientation into the diagonal dominant one.
- **kinds:** Identify what kind of information is represented by the samples along each axis.
- **endian:** Defines whether most significant bytes are found at higher addresses (little) or lower ones (big).
- **encoding:** Describes how the data are formatted.
- **space origin:** Indicates the physical location of the first sample's center within the array.

3 | Code implementation and description

The code used for the computation of the flow inside the nose that is presented is called **tp3d** and is developed in Compiler and Programming Language (CPL). In its original version the code **p3d**, did not include the computation of temperature in the cavity. The idea is to model the flow of the air in the nasal cavities as the flow of a fluid through a three dimensional anisotropic porous medium (from this comes the name given to the code). The conceptual model of flow through a porous medium is that of a flow through a bundle of very small (capillary) tubes of different diameters. For this reason it seemed to be particularly fit for the modelling of the flow inside the nostrils and especially in the *meati*, where the passages can be really small and with a tortuous path.

These kinds of flows are governed by Stokes equation (3.3b). For this reason it is necessary to make a consideration about the reliability of the method. In fact this method would give realistic results only for a flow of air moving at extremely low velocity through the nose. On the other hand the method does not propose to model the flow realistically, but it has the purpose of being useful for medical evaluation of the cavities.

3.1. Governing Equations

In general, for a Newtonian fluid the equations governing the fluid motion can be derived from the conservation laws for mass, momentum (Navier-Stokes equations) and energy, for a material volume (Eq. 3.1)[35]. Considering the problem stationary and incompressible, the equations for mass and momentum can be reduced to Eqs. 3.2a and 3.2b. Applying Boussinesq approximation and considering air modelled as a perfect gas the energy equation is reduced to Eq. 3.2c

$$\begin{cases} \frac{\partial \rho}{\partial t} + \nabla \cdot (\rho \mathbf{u}) = 0 & (3.1a) \\ \rho \left(\frac{\partial \mathbf{u}}{\partial t} + \mathbf{u} \cdot \nabla \mathbf{u} \right) = -\nabla P + \nabla \cdot \left(\mu \left(\nabla \mathbf{u} + (\nabla \mathbf{u})^T - \frac{2}{3} (\nabla \cdot \mathbf{u}) \mathbf{I} \right) \right) + \mathbf{f} & (3.1b) \\ \rho \left(\frac{\partial e}{\partial t} + \mathbf{u} \cdot \nabla e \right) = -\nabla \cdot \mathbf{q}_h - P \nabla \cdot \mathbf{u} + \Phi & (3.1c) \end{cases}$$

$$\begin{cases} \nabla \cdot \mathbf{u} = 0 & (3.2a) \\ \mathbf{u} \cdot \nabla \mathbf{u} = -\frac{1}{\rho} \nabla P + \nu \nabla^2 \mathbf{u} + \frac{\mathbf{f}}{\rho} & (3.2b) \\ \rho c_p \mathbf{u} \cdot \nabla T = -\nabla \cdot \mathbf{q}_h & (3.2c) \end{cases}$$

The flow in the problem is considered to be in Stokes regime, for this kind of flow the Reynolds number is considered sufficiently low, so that the advective inertia forces are negligible compared to the viscous ones. For this same hypothesis the flow is considered mostly laminar and there is no turbulence modelling considered. Volume forces too can be considered null for the problem. With these hypotheses is possible to reduce the momentum equation again to Eq. 3.3b. Supposing that the heat flux follows Fourier law $\mathbf{q}_h = -k_T \nabla T$, the energy equation can be rewritten as in (Eq. 3.3c).

$$\begin{cases} \nabla \cdot \mathbf{u} = 0 & (3.3a) \\ 0 = -\frac{1}{\rho} \nabla P + \nu \nabla^2 \mathbf{u} & (3.3b) \\ \rho c_p \mathbf{u} \cdot \nabla T = \nabla \cdot (k_T \nabla T) & (3.3c) \end{cases}$$

The equation of momentum can be written in the form of Darcy's law for a flow through a porous medium Eq. 3.4b, the mathematical passages to obtain Darcy's from the Stokes equations are shown in [36]. K is the hydraulic conductivity (or medium permeability: since in this study case viscosity is not considered and, hydraulic conductivity $\sigma = \frac{K}{\mu}$ the two are interchangeable). For the nose airway it is necessary to consider a medium with non-homogeneous and anisotropic permeability distribution, for this reason is taken a permeability tensor \mathcal{K} , that take into account the directional variations of the quantity. A more detailed analysis of how the permeability is treated in the medium will be given when describing the code, in section 3.5. The values of specific heat capacity at constant pressure and density, are set unitary, so the thermal conductivity can be considered equal to the thermal diffusivity $k_T = \frac{\alpha}{\rho c_p}$. It is finally possible to write the governing equations

of the system (Eq. 3.4).

$$\left\{ \begin{array}{l} \nabla \cdot \mathbf{u} = 0 \\ \mathbf{u} = -\mathcal{K} \cdot \nabla P \\ \nabla \cdot (k_T \nabla T) + \mathbf{u} \cdot \nabla T = 0 \end{array} \right. \quad \begin{array}{l} (3.4a) \\ (3.4b) \\ (3.4c) \end{array}$$

From the conservation of mass (Eq. 3.4a), and substituting Darcy's law (Eq. 3.4b), we obtain:

$$\nabla \cdot (-\mathcal{K} \cdot \nabla P) = 0 \quad (3.5)$$

Similarly, substituting Darcy's law into Eq. 3.4c, we obtain:

$$\nabla \cdot (k_T \nabla T) - \mathcal{K} \cdot \nabla P \cdot \nabla T = 0 \quad (3.6)$$

It can be observed that Eq. 3.6 is the stationary version of the convection-diffusion equation for flow in a porous medium.

3.1.1. Energy dissipation

A useful quantity for evaluating certain characteristics of the flow in the nose is the rate of energy dissipation per unit volume ϵ . To compute this, it is necessary to start from the definition of ϵ for an incompressible flow through a porous medium. In a porous medium, the rate of energy dissipation is associated with the pressure drop across the medium (Eq. 3.7a). Substituting Darcy's velocity \mathbf{u} (3.4b), it is possible to write Eq. 3.7b.

$$\epsilon = \mathbf{u} \cdot \nabla P \quad (3.7a)$$

$$\epsilon = -\mathcal{K} |\nabla P|^2 \quad (3.7b)$$

3.2. Hele-Shaw model

For the computation of the hydraulic conductivity in the nose airways, will be used a model based on Hele-Shaw flow. Hele-Shaw is a flow taking place between two parallel flat plates separated by a really narrow gap (Fig. 3.1). x and y are the directions parallel to the flat plates and z is the perpendicular direction. h is the gap between the two plates.

The condition to be satisfied for this kind of flow is:

$$Re \frac{h}{l} \ll 1 \quad (3.8)$$

Where $Re = uh/\nu$ is the Reynolds number and l is the characteristic length scale in directions parallel to the plate. This way the flow satisfies Stokes equations (3.3b), imposing no-slip and no-penetration boundary conditions at $z = 0$ and $z = h$ it is possible to write the components of velocity as in Eqs. 3.9. Where again viscosity is ignored.

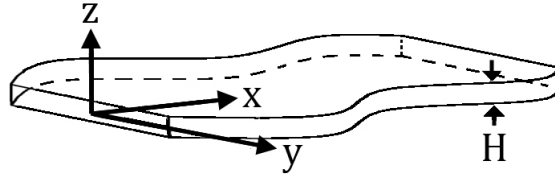


Figure 3.1: Hele-Shaw configuration

$$\begin{cases} v_x = -\frac{1}{2} \frac{\partial p}{\partial x} z(h-z) & (3.9a) \\ v_y = -\frac{1}{2} \frac{\partial p}{\partial y} z(h-z) & (3.9b) \\ v_z = 0 & (3.9c) \end{cases}$$

It is immediate to see that this flow can be described using Darcy's law, for a flow in a porous medium (Eq. 3.4). The conductivity changes only along the width of the channel and is defined as:

$$K(z) = \frac{z}{2}(h-z) \quad (3.10)$$

In a Hele-Shaw channel it is possible to consider the depth-averaged form of any physical quantity (Eq. 3.11).

$$\langle \phi \rangle = \frac{1}{h} \int_0^h \phi dz \quad (3.11)$$

It is then possible to define a depth averaged hydraulic conductivity as in Eq. 3.12.

$$\langle K \rangle = \frac{h^2}{12} \quad (3.12)$$

3.3. Airway geometry and bounding box

The initial task executed by **tp3d** involves reading the NRRD file and extracting the necessary information to conduct Computational Fluid Dynamics (CFD) simulations on the airway. A three-dimensional array of integers is constructed where each element represents the radiodensity of the corresponding voxel, measured in Hounsfield Units (HU).

Subsequent to array construction, the algorithm proceeds to isolate the airway structure from the larger dataset. This isolation process entails defining a rectangular parallelepiped bounding box. This bounding box delineates the specific computational domain of interest within the volumetric data.

The computational framework delineates the airway structure within the volumetric domain through a systematic approach, described as follows:

1. The bounding box (BB) initialization aligns with the dimensions of the entire domain under consideration, ensuring the anatomical structure is entirely contained inside the box.
2. A method is employed to identify the tip of the nose, utilizing the radiodensity threshold in Hounsfield Units imposed (HU_{thr}). This involves iteratively scanning voxel values in all three directions, analyzing each y -plane going in the positive direction, stopping upon encountering the first voxel where $HU > HU_{thr}$. Subsequently, the detected position is refined by iterating both in forward and backward directions along x to ensure precise centering of the nose tip.
3. The lower z -boundary of the bounding box is determined by enforcing a specified distance from the nose tip. This device is used to consider the airway in the same way for all the CTs.
4. A depth function is applied, commencing from the maximal y value. This function quantifies the distance in the y direction until the first boundary between solid and fluid phases (or vice versa) is encountered. The results from the application of this function can be visualized in Fig. 3.2, where the scale of colors is used to give the depth dimension (yellow closest to the observer).
5. It is then created a new array of integer values **connectmap** with the dimensions of the array of voxels. To each element of **connectmap** is assigned a binary value: 1 for voxels with $HU \leq HU_{thr}$ (indicative of air or active voxels) and 0 for all the others (solid or barrier voxels).
6. A region beneath each nostril is generated by extrapolating a square in the y direc-

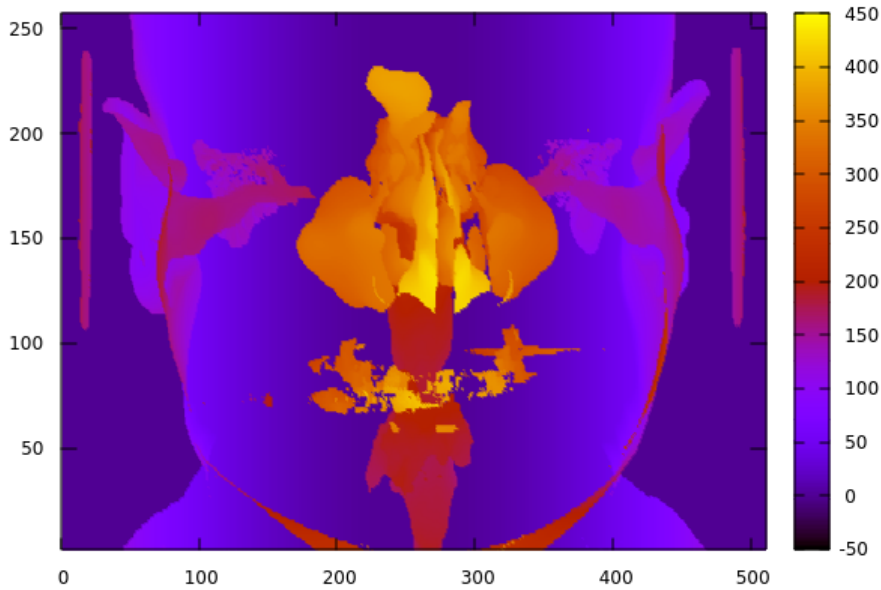


Figure 3.2: 2D representation of the patient based on depth function

tion, from $y = 0$ to the solid-air boundary (face surface), based on the previously determined nose-lip distance and nose tip position, and scaled according to the **space directions**. Here the boundary is defined simply by the threshold imposed, where voxels with radiodensity value lower than the threshold represent air, and voxels with value higher than the threshold define the solid volume.

7. Subsequently, all exterior voxels with a value of 1 that lie outside the head and the delineated volume are reassigned a value of 0, excluding them from further computational analysis.
8. A connectivity routine is utilized to identify simply connected regions within the volume. Replacing 1s in **connectmap** with consecutive integers to enumerate connected active regions, so that all the elements belonging to the connected airway are assigned the same value. This routine simply checks the value of each element in the 3D array and if it is equal to 1, checks the values of the neighbouring elements, building a list of elements that are adjacent and associating same value N in the array to all of them.
9. By selecting a reference point within the airway volume, all other connected regions are excluded, isolating the airway's connected region for focused analysis Fig. 3.3. If this element is assigned value zero it's because the program could not recognize

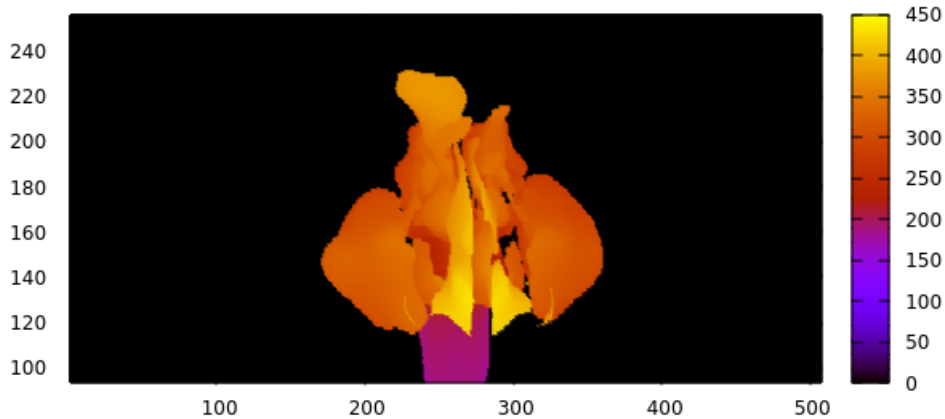


Figure 3.3: Isolated airway

the connected airway, so it stops automatically.

10. The bounding box is finally refined to encompass the minimum and maximum x values of the connected airway region, y extending from 0 to the region's maximal value, and z spanning from the predefined lower boundary to the connected region's uppermost point.

3.4. Definition of the airways boundary

An algorithm is introduced that computes the real distances between each voxel and the closest solid walls in three directions. These values are essential for the computation of hydraulic conductivity, as will be shown in the next section. This procedure is performed using the *STARLINE* subroutine.

This iterative process examines every line of voxels within the bounding box. For each voxel, it computes the distance from the closest boundary in each direction and each orientation.

Ensuring a precise delineation between the solid and fluid domains is critical, especially when considering airway structures with narrow passages. The differentiation between these domains cannot be coarse, with precision limited to the order of a single voxel. To overcome this limitation and achieve greater precision and definition, *STARLINE* incorporates an interpolation technique at the boundary. This approach enables a more precise localization of the interface between what is considered solid and air. The subroutine *STARLINE* includes an inline subroutine *UPDPOS* (Algorithm 3.1) for this purpose. When crossing the threshold value from barrier to active voxels along a line, *UPDPOS* is triggered.

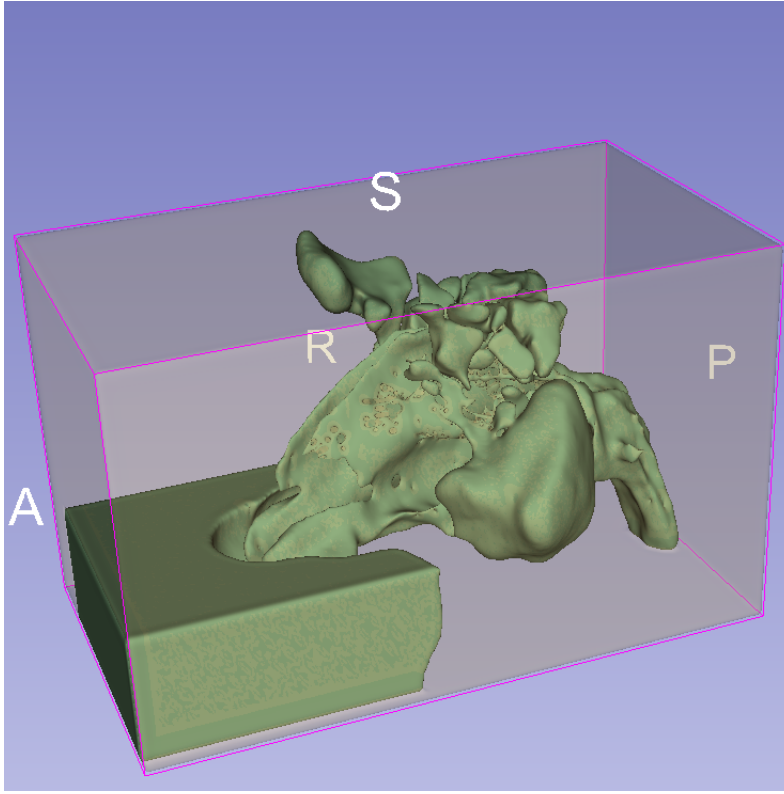


Figure 3.4: Bounding box and connected region

Algorithm 3.1 Computation of the interface with *UPDPOS*

```

oldvox = newvox
newvox = HUthr - HU(i)
if newvox ≥ 0 and oldvox < 0 then
  bottom = HUthr
  repeat
    until i out of Bounding Box boundaries or HU(i) > bottom
    bottom = HU(i)
    i = i + di
  until CONDITION

```

$$\Delta_{thr} = -500 - HU_{thr} + 500\sqrt{2} \left(1 - \frac{bottom}{(-1000)}\right)^3 \quad (3.13)$$

$$intf_{pos} = d_p - d_p \cdot MIN \left(1, \frac{newvox + \Delta_{thr}}{newvox - oldvox}\right) \quad (3.14)$$

```

end if

```

The steps of the algorithm can be summarized as follows:

1. **Initialization: oldvox** and **newvox** are defined as the differences between the imposed radiodensity threshold HU_{thr} and the radiodensity of the considered voxel, named HU , respectively for the element before and after passing the threshold iterating along the line. i is the coordinate on the axis considered and d_i its unit displacement.
2. **Finding the bottom voxel**: Starting from the first voxel after passing the threshold, the algorithm iterates along the line of voxels until it identifies the **bottom** voxel, which is the voxel where the gradient of radiodensity in the considered direction changes sign and becomes positive.
3. **Computing the correction value** Δ_{thr} (Eq. 3.13): This is based on the values of HU_{thr} and **bottom**.
4. **Computing the displacement of the new interface with respect to the original one** as in Eq. 3.14.

A visual representation of the process is given in Fig. 3.5, where red rectangles represent barrier voxels (radiodensity higher than the imposed threshold), while green rectangles represent active voxels (radiodensity lower than the imposed threshold). Darker shades indicate lower radiodensity, and green voxels always have a lower radiodensity than red ones.

Omitting the term Δ_{thr} results in a simple first-order interpolation at the boundary. Given that the passageways can be extremely narrow, this can significantly impact the results, as will be demonstrated in Section 4.3. This type of interpolation is designed to accurately identify an airway, making the imposed threshold crucial for delineating the interface precisely.

It is important to note that the boundary definition is realized by considering only the voxels on the same line.

With these two subroutines, every active voxel in the bounding box is associated with six real values representing the lengths of the segments connecting it to the closest boundary in each principal direction and orientation. The computed values considering respectively positive and negative orientation are called $STAR(x_i, 0)$ and $STAR(x_i, 1)$, for each direction $x_i = [x, y, z]$. These values will be used in the next section for the computation of the hydraulic conductivity.



Figure 3.5: Computation of the position of the interface

3.5. Hydraulic conductivity

Since the governing equation considered are the ones for a flow in a porous medium, a key aspect of the problem is the numerical computation of the hydraulic conductivity. The whole bounding box is considered as a porous medium and each voxel will be assigned a scalar value of conductivity, that is computed building a model based on Hele-Shaw flow (Section 3.2)[37].

What is done in practice is evaluating the definite integral of the conductivity between the solid boundaries on each voxel, then dividing for the length of the voxels' side, to take into account the dimension of the voxels in each direction. The indefinite integral is written as in Eq. 3.15 when considering the parabolical conductivity profile (Eq. 3.10), or like in Eq. 3.16 for the flat conductivity profile (Eq. 3.12).

$$Q_{par} = x_i^2 \left(\frac{h}{4} - \frac{x_i}{6} \right) \quad (3.15)$$

$$Q_{flat} = x_i \frac{h^2}{12} \quad (3.16)$$

$$x_i = [x, y, z]$$

It is to remark that, using Q_{par} for the computations on a simple geometry, as in Hele-Shaw and Hagen-Poiseuille flow, it should be possible to obtain the exact solution, with an error introduced only by the discretization. For this reason the code was tested on a circular cylinder in section 4.1.

The calculation of the directional contribution to conductivity in a single voxel, is realized as shown below. The idea for the computation of conductivity is to take either Q_{par} or Q_{flat} integral and redistribute it along the width of the channel depending on the distance from the boundary in the three directions.

1. $a_{x_i} < 0$ or $b_{x_i} - a_{x_i} < 0$. The considered voxel is inactive and is thus assigned a null value of conductivity

$$K_{x_i}(i_x, i_y, i_z) = 0$$

2. $a_{x_i} + dim_{x_i} < b_{x_i}$ and $a_{x_i} - dim_{x_i} > 0$. For voxels that are not in close proximity to the boundary in either orientation (Fig. 3.7).

$$K_{x_i}(i_x, i_y, i_z) = \frac{1}{dim_{x_i}} [Q]_{a_{x_i} - \frac{dim_{x_i}}{2}}^{a_{x_i} + \frac{dim_{x_i}}{2}}$$

3. $a_{x_i} + dim_{x_i} < b_{x_i}$ and $a_{x_i} - dim_{x_i} \leq 0$. For points located less than one voxel's width away from the first solid boundary in the considered direction (Fig. 3.8).

$$K_{x_i}(i_x, i_y, i_z) = \frac{1}{dim_{x_i}} [Q]_0^{a_{x_i} + \frac{dim_{x_i}}{2}}$$

4. $a_{x_i} + dim_{x_i} \geq b_{x_i}$ and $a_{x_i} - dim_{x_i} > 0$. For points located less than one voxel's width away from the second solid boundary in the considered direction (Figs. 3.9).

$$K_{x_i}(i_x, i_y, i_z) = \frac{1}{dim_{x_i}} [Q]_{a_{x_i} - \frac{dim_{x_i}}{2}}^{b_{x_i}}$$

5. $a_{x_i} + dim_{x_i} \geq b_{x_i}$ and $a_{x_i} - dim_{x_i} \leq 0$. For cases where the width of the channel is smaller than that of the single voxel, necessitating the consideration of the entire integral of conductivity (Fig. 3.10).

$$K_{x_i}(i_x, i_y, i_z) = \frac{1}{dim_{x_i}} [Q]_0^{b_{x_i}}$$

$$x_i = [x, y, z]$$

Where the values represented also in Fig.3.6 are:

- dim_{x_i} is the length of the side of the voxel in the direction x_i considered.
- a_{x_i} is the distance between the voxel and the boundary in the positive direction of the axis, corresponding to $STAR(x_i, 0)$.
- b_{x_i} is the total distance between the boundaries of the airway in that direction, computed as the sum of a_{x_i} and the distance between the voxel and the closest boundary in the negative orientation of the axis considered $STAR(x_i, 1)$.

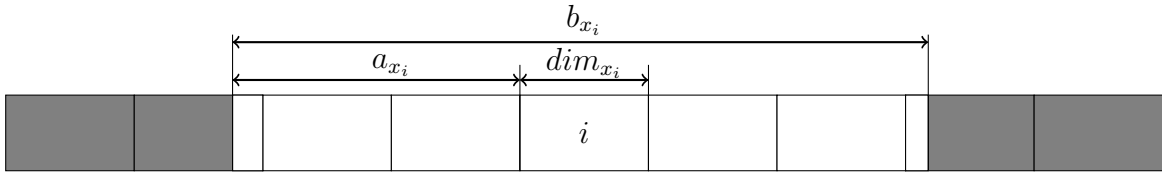


Figure 3.6: Representation of the distances derived from *STARLINE* used for the computation of conductivity

Once computed the three directional contributions to conductivity, it is taken the harmonic sum of the K components to synthesize a comprehensive measure of conductivity in each voxel. The harmonic sum, is a function defined as $h_{sum}(x, y) = xy/(x + y)$. The result of this process is shown in Eq. 3.17.

$$K(i) = \frac{K_x(i)K_y(i)K_z(i)}{K_x(i)K_y(i) + K_y(i)K_z(i) + K_x(i)K_z(i)} \quad (3.17)$$

$$i = [i_x, i_y, i_z]$$

With this approach the airway is defined as a porous medium with a scalar value of hydraulic conductivity assigned in each voxel. To consider the different directional components in the permeability tensor, is sufficient to compute the average between the conductivity in a voxel and the adjacent ones, as will be shown when calculating the numerical solution for the field of pressure (section 3.6).

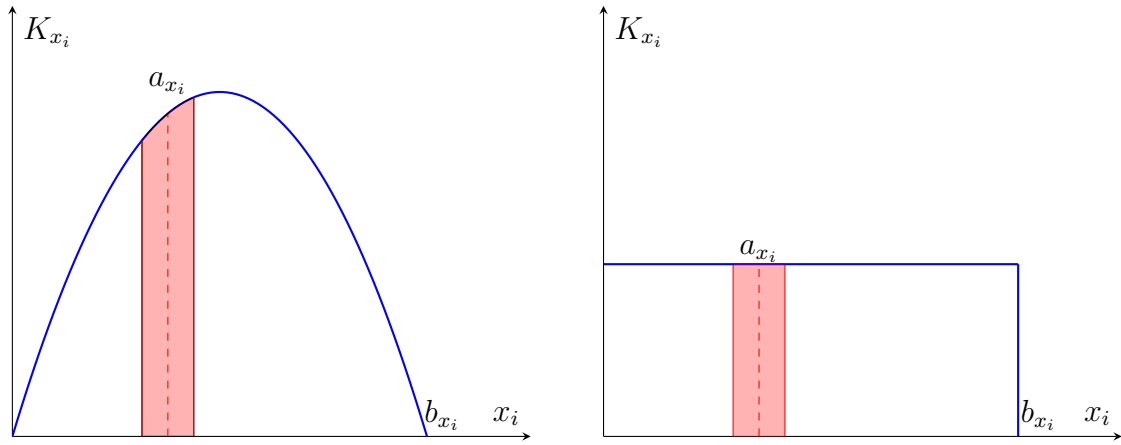


Figure 3.7: Definite integral visualization for $a_{x_i} + \dim_{x_i} < b_{x_i}$ and $a_{x_i} - \dim_{x_i} > 0$

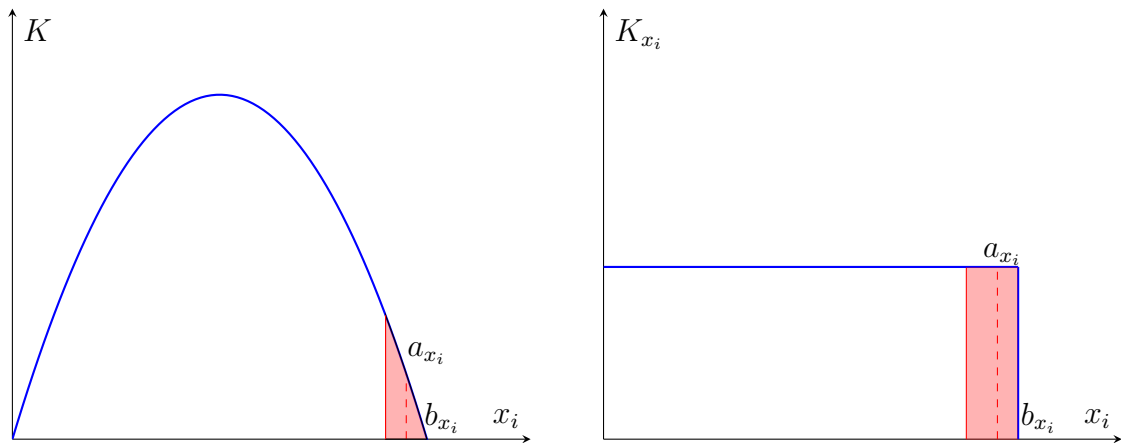


Figure 3.8: Definite integral visualization for $a_{x_i} + \dim_{x_i} \geq b_{x_i}$ and $a_{x_i} - \dim_{x_i} > 0$

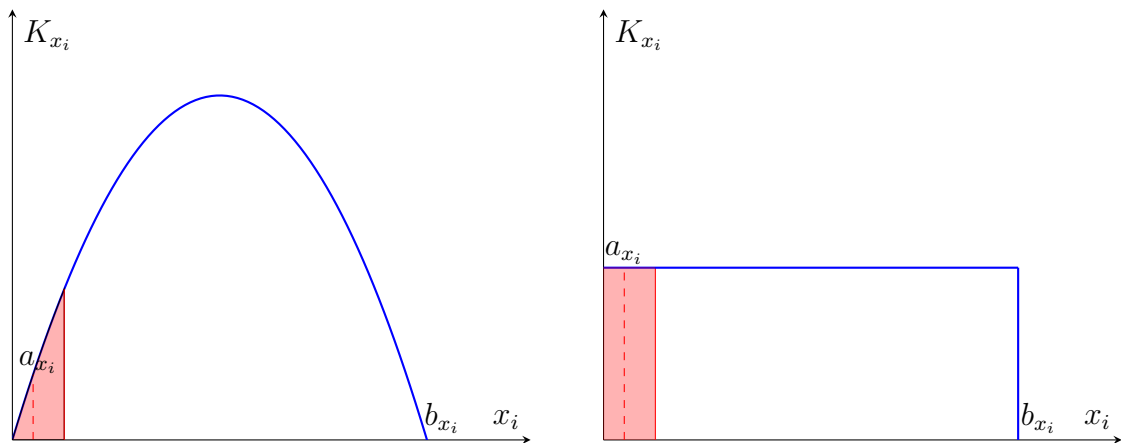


Figure 3.9: Definite integral visualization for $a_{x_i} + \dim_{x_i} < b_{x_i}$ and $a_{x_i} - \dim_{x_i} \leq 0$

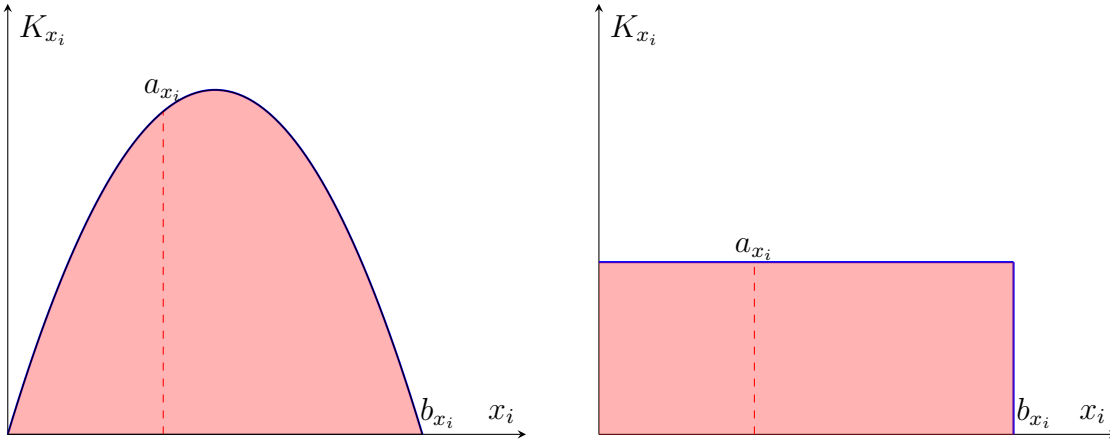


Figure 3.10: Definite integral visualization for $a_{x_i} + dim_{x_i} \geq b_{x_i}$ and $a_{x_i} - dim_{x_i} \leq 0$

3.6. Pressure field

3.6.1. Initial Conditions

The pressure field initialization involves assigning a value of 1 [Pa] to active voxels, whereas solid volume voxels are assigned a value of $P = -0.199$ [Pa]. For the voxels on the lower boundaries in the y and z directions of the region outside the nose, the value 1 is fixed. This surface constitutes the system inlet. Active voxels located on the bounding box's lower boundary in the z -direction, within the throat region, are set to $P = 0$ [Pa] to impose the pressure jump between the external air and the throat.

3.6.2. Numerical solution

Once the initial pressure values and conductivity values are assigned to every element in the volume, it is possible to numerically compute the pressure field. This is done using a method to calculate a solution that satisfies Eq. 3.5. In this method, is evaluated the balances of the fluxes (in this case volumetric flow rate) on each finite volume.

For the sake of fast numerical convergence, a multigrid method is employed [38], using a red-black Successive Over-Relaxation (SOR) method for smoothing [39]. This approach aims for efficient parallelization and faster convergence compared to a simple Gauss-Seidel method [40]. The steps reproduced at each iteration in the smoothing step of the multigrid for the computation of pressure can be summarized as follows:

The computations continue until the quantity *Residual* (Eq.3.23) reaches a value below a certain threshold imposed or when passing a maximum number of iterations. The cases for which the solution does not converge properly are excluded from the results.

Algorithm 3.2 Iterative method for the computation of pressure

for All active voxels i **do**

$$P_R(i) = \sum_{n \in \mathcal{N}} \left((K(i+n) + K(i)) \frac{A_n}{\Delta_n} \right) P(i+n) \quad (3.18)$$

$$c_{00}(i) = \sum_{n \in \mathcal{N}} \left((K(i+n) + K(i)) \frac{A_n}{\Delta_n} \right) \quad (3.19)$$

$$P_{resid}(i) = P_R(i) - c_{00}(i)P(i) \quad (3.20)$$

$$P_{new}(i) = \omega \frac{P_{resid}(i)}{c_{00}(i)} + (1 - \omega)P(i) \quad (3.21)$$

$$P(i) = P_{new}(i) \quad (3.22)$$

end for

$$Residual = \sqrt{\sum_{i_x=2}^{n_x-1} \sum_{i_y=2}^{n_y-1} \sum_{i_z=2}^{n_z-1} P_{resid}(i)} \quad (3.23)$$

Where:

- $i = (i_x, i_y, i_z)$ denotes the indices of the current voxel in vector form.
- \mathcal{N} represents the set of neighboring voxel offsets n , with $\mathcal{N} = \{(-1, 0, 0), (1, 0, 0), (0, -1, 0), (0, 1, 0), (0, 0, -1), (0, 0, 1)\}$.
- A_n is the area of the face perpendicular to the direction of n : A_{yz} , A_{xz} , or A_{xy} and Δ_n is the voxel dimension in the direction of n , either Δx , Δy , or Δz . The ratio between these two terms is used to take into account the directional weight of every contribution, that depends on the dimensions of the voxels.
- P is the value of pressure in the point computed in the precedent iteration. For the first iteration the values are the ones imposed.
- P_R and c_{00} are two variables calculated to impose the flux balance at each cell.
- P_{resid} is the residual computed in each point.
- ω is the relaxation factor and is set to a value of 1.5

3.7. Velocity and Energy dissipation rate

Once the fields of pressure and conductivity are obtained it is straightforward to derive the velocity and the energy dissipation rate ϵ .

To visualize the airflow inside the cavities, a method is implemented to compute the velocity components and magnitude within the airways. The velocity components can be derived directly from Eq. 3.4b. To assign a value to each voxel, central differences are considered for the velocity of the flow in each cell in the specified direction.

$$u_{x_i}(i) = \frac{\frac{K(i)+K(i+d)}{2} \left(P(i+d) \right) - P(i) - \frac{K(i)+K(i-d)}{2} \left(P(i-d) - P(i) \right)}{2\Delta d} \quad (3.24)$$

The velocity magnitude field is computed as:

$$u_{mag}(i) = \sqrt{u_x(i)^2 + u_y(i)^2 + u_z(i)^2} \quad (3.25)$$

Exploiting Eq. 3.7b, the rate of energy dissipation can be computed numerically at every active point as:

$$\epsilon(i) = K(i) \sum_{d \in \{dx, dy, dz\}} \left(\frac{P(i+d) - P(i-d)}{2\Delta d} \right)^2 \quad (3.26)$$

Where:

- $i = (i_x, i_y, i_z)$ denotes the index vector of the voxel considered.
- d represents the directional unit displacements $dx = (1, 0, 0)$, $dy = (0, 1, 0)$, and $dz = (0, 0, 1)$, corresponding to each spatial dimension.
- Δd refers to the voxel dimension in the direction of d .
- $P(i+d)$ and $P(i-d)$ denote the pressure at the voxels offset by one unit in the positive and negative directions of d , respectively.
- x_i is an index denoting the component of the velocity considered $x_i = (x, y, z)$

3.8. Flow of air in the nostrils and the throat

The flow of air in each nostril (Eqs. 3.27b and 3.27c), is computed starting from the faces of the geometry defined outside the nose where the value of pressure $P = 1$ has been imposed (inlet). The flow of air at the interface of the cells is computed numerically by applying the integral form of Eq. 3.4b.

To accurately account for the distribution of the flow in the two nostrils, the flow of air from the left to the right side of the sagittal plane passing through the nose tip is also computed (as indicated in Eq. 3.27a). This adjustment is reflected in the total flow rate calculations for each nostril, with the computed value added to the total flow in the right nostril and subtracted from the total flow in the left nostril. This procedure is applied so that the flow rate is computed correctly for every patient in the database. Similarly, the flow of air in the throat (Eq. 3.27d) is computed in the same manner as for Eqs. 3.27b and 3.27c, utilizing the imposed boundary condition (BC) of $P = 0$ in the throat.

It is important to note that $K \neq 0$ only inside the connected region.

$$Q_{LR} = A_{yz} \sum_{i_y=2}^{n_{tip(y)}} \sum_{i_z=2}^{n_{tip(z)}-1} \frac{K(n_{tip(x)}, i_y, i_z) + K(n_{tip(x)} - 1, i_y, i_z)}{2} \cdot \frac{P(n_{tip(x)} - 1, i_y, i_z) - P(n_{tip(x)}, i_y, i_z)}{\Delta x} \quad (3.27a)$$

FOR $p(ix, iy, 1) \neq 0$

$$Q_{RN} = A_{xy} \sum_{i_x=2}^{n_{tip(x)}-1} \sum_{i_y=2}^{n_y-1} \frac{K(i_x, i_y, 1) + K(i_x, i_y, 2)}{2} \frac{P(i_x, i_y, 1) - P(i_x, i_y, 2)}{\Delta z} + A_{xz} \sum_{i_x=2}^{n_{tip(x)}-1} \sum_{i_z=2}^{n_z-1} \frac{K(i_x, 1, i_z) + K(i_x, 2, i_z)}{2} \frac{P(i_x, 1, i_z) - P(i_x, 2, i_z)}{\Delta y} + Q_{LR} \quad (3.27b)$$

$$Q_{LN} = A_{xy} \sum_{i_x=n_{tip(x)}}^{n_x-1} \sum_{i_y=2}^{n_y-1} \frac{K(i_x, i_y, 1) + K(i_x, i_y, 2)}{2} \frac{P(i_x, i_y, 1) - P(i_x, i_y, 2)}{\Delta z} + A_{xz} \sum_{i_x=n_{tip(x)}}^{n_x-1} \sum_{i_z=2}^{n_z-1} \frac{K(i_x, 1, i_z) + K(i_x, 2, i_z)}{2} \frac{P(i_x, 1, i_z) - P(i_x, 2, i_z)}{\Delta y} - Q_{LR} \quad (3.27c)$$

FOR $p(i_x, i_y, 1) = 0$

$$Q_{TH} = A_{xy} \sum_{i_x=2}^{n_x-1} \sum_{i_y=2}^{n_y-1} \frac{K(i_x, i_y, 1) + K(i_x, i_y, 2)}{2} \frac{P(i_x, i_y, 1) - P(i_x, i_y, 2)}{\Delta z} \quad (3.27d)$$

For the output results, it is decided to normalize the volumetric flow rates by taking the unitary flow in the throat.

$$\left\{ \begin{array}{l} \Delta P_{\text{new}} = \frac{1}{Q_{\text{TH}}} \quad (3.28a) \\ P_{\text{new}} = P \Delta P_{\text{new}} \quad (3.28b) \\ Q_{\text{RN new}} = Q_{\text{RN}} \Delta P_{\text{new}} \quad (3.28c) \\ Q_{\text{LN new}} = Q_{\text{LN}} \Delta P_{\text{new}} \quad (3.28d) \\ Q_{\text{TH new}} = Q_{\text{TH}} \Delta P_{\text{new}} \quad (3.28e) \end{array} \right.$$

All these results are reported on a txt file named "flowrate.txt".

3.9. Temperature

To compute the temperature field, it is necessary to include the energy equation as a governing equation. The equation for the conservation of energy that will be utilized is Eq. 3.6. The temperature is considered adimensional.

3.9.1. Initial Conditions

The boundary conditions for temperature are imposed similarly to those for pressure. The temperature at the boundaries is set to $T_B = 10^{-4}$ for all barrier voxels. All active points are initialized with a temperature $T(i_x, i_y, i_z) = \frac{P(i_x, i_y, i_z)}{\Delta P}$, ensuring that the imposed jump in temperature is equal to the one in pressure.

3.9.2. Thermal Conductivity

The thermal conductivity is determined directly from the values of hydraulic conductivity as shown in Eq. 3.29. It is considered to have opposite behavior along the width of the channel. $K_{T \text{ Cost}}$ is defined empirically and depends on the dimensions of the voxels.

$$\begin{cases} k_T \text{ Cost} = \Delta x \Delta y \Delta z \cdot 3 \cdot 10^{-4} & (3.29a) \\ k_T(i) = \frac{k_T \text{ Cost}}{K(i)} & (3.29b) \end{cases}$$

3.9.3. Numerical Solution

The computation of the temperature field leverages, imposes the balance of heat flux in every voxel. The method for computing temperature is similar to that used for pressure, with the main difference being the inclusion of an additional term, the thermal conductivity one (k_T).

Since a fast convergence is not an issue in this phase, the numerical method is applied without the use of multigrid and SOR. The iterative procedure is executed across every active voxel in both forward and backward directions. The steps for computing temperature are detailed in Algorithm 3.3. The iterative process continues until the value of T_{resid} falls below 10^{-6} in every active voxel.

Algorithm 3.3 Iterative method for the computation of temperature

for All active voxels i **do**

$$\begin{aligned} T_R(i) = & \sum_{n \in \mathcal{N}^-} \left((K(i+n) + K(i)) \frac{(P(i+n) - P(i)) A_n}{\Delta_n} \right) T(i+n) - \\ & - \sum_{n \in \mathcal{N}^+} \left((K(i+n) + K(i)) \frac{(P(i+n) - P(i)) A_n}{\Delta_n} \right) T(i+n) \end{aligned} \quad (3.30)$$

$$\begin{aligned} c_{00}(i) = & \sum_{n \in \mathcal{N}^-} \left((K(i+n) + K(i)) \frac{(P(i+n) - P(i)) A_n}{\Delta_n} \right) - \\ & - \sum_{n \in \mathcal{N}^+} \left((K(i+n) + K(i)) \frac{(P(i+n) - P(i)) A_n}{\Delta_n} \right) \end{aligned} \quad (3.31)$$

$$T(i) = \frac{T_R(i)}{c_{00}(i) + k_T(i)} \quad (3.32)$$

$$T_{resid}(i) = T_R(i) - \left(c_{00}(i) + k_T(i) \right) T(i) \quad (3.33)$$

end for

- \mathcal{N}^- represents the set of neighboring voxel offsets n , with $\mathcal{N}^- = \{(-1, 0, 0), (0, -1, 0), (0, 0, -1)\}$.

- \mathcal{N}^+ represents the set of neighboring voxel offsets n , with $\mathcal{N}^+ = \{(1, 0, 0), (0, 1, 0), (0, 0, 1)\}$.
- T_R and c_{00} are two variables calculated to impose the flux balance at each cell.
- T is the value of temperature computed at each iteration in each voxel.
- T_{resid} is the residual in the computation of temperature in each voxel.

3.10. Heat transfer and temperature in the throat

After establishing the temperature field, the heat transfer H_{TH} in the throat is determined using Eq. 3.34. As with the computation of the volumetric flow rate in the throat (Eq. 3.27d), is considered only the flux in the voxels on the lower z -boundary of the bounding box, which have been assigned a value of 0. When the flow rate in the throat is set to unity, the value of the heat transfer directly corresponds to the average temperature in the throat, i.e., $H_{TH} = T_{TH}$.

$$H_{TH} = A_{xy} \sum_{i_x=2}^{n_x-1} \sum_{i_y=2}^{n_y-1} \frac{K(i_x, i_y, 1) + K(i_x, i_y, 2)}{2} \cdot \frac{P(i_x, i_y, 2) - P(i_x, i_y, 1)}{\Delta z} (T(i_x, i_y, 2) - T(i_x, i_y, 1)) \quad (3.34)$$

$$H_{TH} = Q_{TH} T_{TH} \quad (3.35)$$

The values of H_{TH} and T_{TH} are also printed in "flowrate.txt".

3.11. Representation of the results

To visualize the fields of pressure, permeability, rate of energy dissipation, and temperature, NRRD files are generated from their respective computed 3D arrays. This process involves converting the real-valued computations in each voxel to integer values and writing them alongside the header information that characterizes the file. The steps are as follows:

- Define d_{max} as the maximum absolute value within the array.
- Compute $NORM = \frac{10000}{d_{max}}$.
- Rewrite each element in the array as $P(i) = ROUND(NORM \cdot P(i))$, where $ROUND$ is

a CPL built-in function that rounds the value inside the parenthesis to the nearest integer.

This procedure generates a NRRD file containing signed 2-byte integers. All computational results for **tp3d** and discussed in the subsequent chapters are obtained through this process.

4 | Tests and preliminary results

4.1. Test on simple geometry

In order to verify the proper functionality and correct usage of the **tp3d** code, a test is conducted on a simple geometry. In this case, a straight cylinder is used, for which the theoretical solution for Stokes flow is provided by the Hagen-Poiseuille equation [41].

The Hagen-Poiseuille equation is derived from the momentum equation for Stokes flow in 3D cylindrical coordinates. Considering the axial coordinate z and the radial coordinate r , the momentum equation can be written as shown in Eq. 4.1:

$$\frac{1}{r} \frac{\partial}{\partial r} \left(r \frac{\partial u}{\partial r} \right) = \frac{dP}{dz} \quad (4.1)$$

To generate the shape of the cylinder, a 3D array of integers is written in the CPL environment, and the desired radiodensity value is assigned to each element (Algorithm 4.1). To build the NRRD file, the same process used for generating the results (Section 3.11) is applied, with modifications to associate a radiodensity value to each voxel.

Considering the cylinder to be filled with air, the radiodensity value assigned to each element inside the volume is $HU = -1000$. Elements outside are assigned $HU = 0$, while elements on the boundary have a value based on the real distance from the center, ranging between -1000 and 0. The height of the cylinder is determined by defining the number of elements in the array along the z -direction and setting the voxel sizes in the NRRD header definition.

The entire process that defines the airway for the noses (Section 3.3) is simplified to distinguish between the air inside the cylinder and the shape of the cylinder.

Given that the purpose is to obtain a Hagen-Poiseuille flow, the conductivity is computed with the correspondent integral of velocity (Eq. 3.15). Furthermore, the calculation of the contribution to permeability in the direction of the length of the cylinder is not considered, in fact, since the cylinder is open on both sides every point is considered to be at infinite

Algorithm 4.1 Cylinder geometry definition

Require: Definition of the array dimensions and of the voxel size in the three directions
 Position of the center of the circular section of the cylinder ($center_x, center_y$) and value of the radius (R)

for Each element i_x, i_y, i_z contained inside the array **do**
 $distance = \sqrt{((i_x - center_x)\Delta_x)^2 + ((i_y - center_y)\Delta_y)^2}$
 if CEILING($distance$) < R **then**
 $HU(i_x, i_y, i_z) = -1000$
 else if CEILING($distance$) = R **then**
 $HU(i_x, i_y, i_z) = -1000|R - distance|$
 else
 $HU(i_x, i_y, i_z) = 0$
 end if
end for

distance from the boundaries in the axial direction. For this reason, the correspondent directional contribution of conductivity will be infinite. Adding an infinite term to the harmonic sum (Eq. 3.17) does not change its value, as shown in Eq. 4.2.

$$K(i) = \lim_{K_z \rightarrow \infty} \frac{K_x(i)K_y(i)K_z(i)}{K_x(i)K_y(i) + K_y(i)K_z(i) + K_x(i)K_z(i)} = \frac{K_x(i)K_y(i)}{K_x(i) + K_y(i)} \quad (4.2)$$

$$i = [i_x, i_y, i_z]$$

The boundary conditions are imposed in the same manner as for the airway, with $P = 0$ [Pa] at the outlet and $P = 1$ [Pa] at the inlet, and all elements inside the cylinder initialized with $P = 1$ [Pa]. The grid considered for the computations is structured, where each voxel is cubic with a side length of $\Delta = 0.5$ mm.

The quantities compared with the theoretical case are the volumetric flow rate Q , the velocity component in the z -direction \mathbf{v}_z , and the pressure distribution in the axial direction.

A cylinder of length $L = 250$ mm is considered and tested for various values of radius R . For the Hagen-Poiseuille flow, the volumetric flow rate is computed as in Eq. 4.3, which is derived directly from Eq. 4.1. The geometry is extrapolated by imposing a radiodensity threshold of -500 HU, to obtain a sufficiently smooth geometry with the correct radius value.

$$Q_{theory} = \frac{\Delta P \pi R^4}{8L} \quad (4.3)$$

For each radius value it is also computed the value of the percentual error with respect

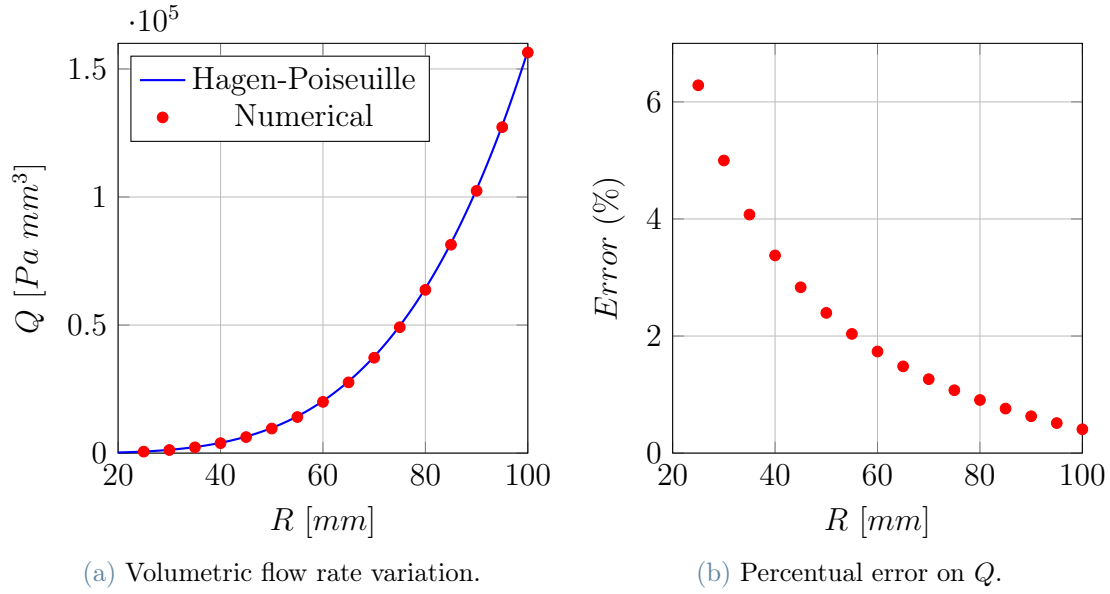


Figure 4.1: Results for the volumetric flow rate at various radii.

to the theoretical case.

$$Error(\%) = \frac{|Q_{theory} - Q_{num}|}{Q_{theory}} 100 \quad (4.4)$$

To confirm the flow behaves like a Hagen-Poiseuille one, it is also visualized the comparison with the theoretical velocity profile, which is described by the law:

$$v_z(y) = \frac{\Delta P}{4L} (R^2 - y^2) \quad (4.5)$$

The results from the theoretical and computational methods are comparable. The error in the volumetric flow rate decreases as the radius of the cylinder increases (Fig. 4.1). The velocity exhibits a similar behavior. As shown in Fig. 4.2, although both velocity profiles approximate the theoretical one well, the profile for the larger radius provides better results. The pressure distribution along the height of the solid volume demonstrates the expected linear behavior (Fig. 4.3).

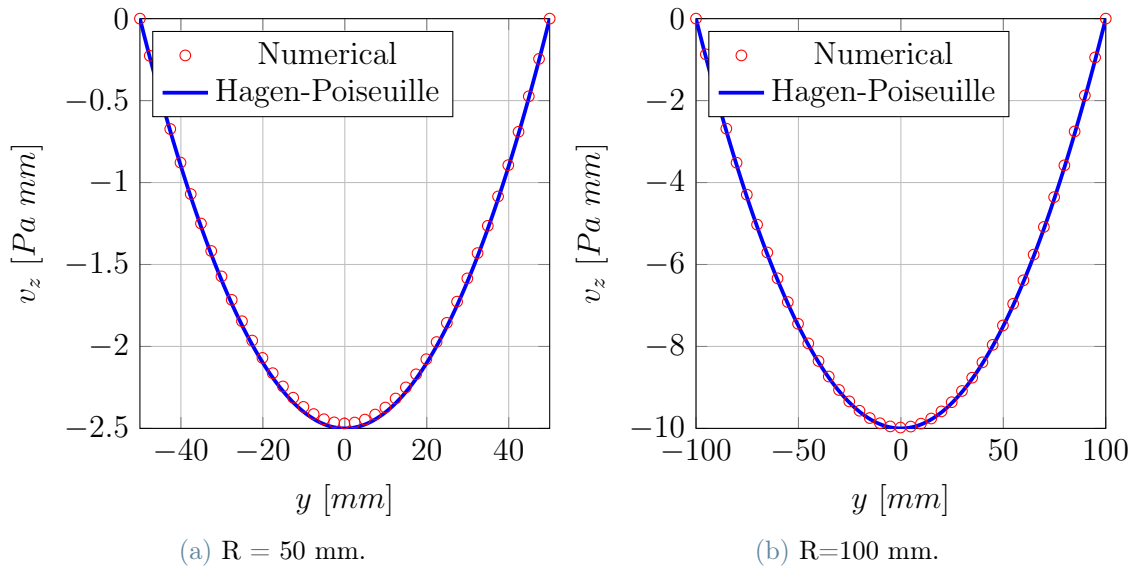


Figure 4.2: Velocity profile

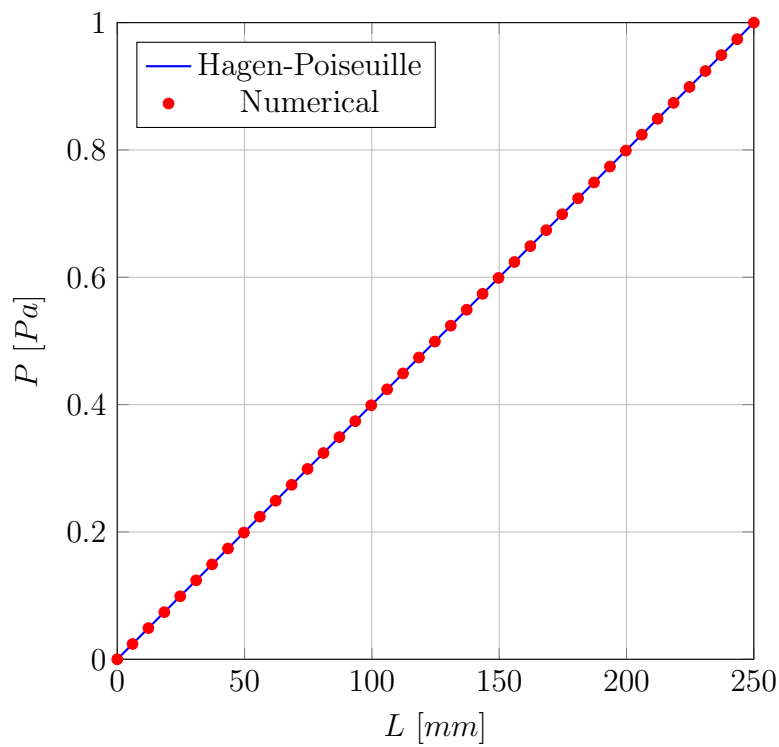


Figure 4.3: Pressure variation with cylinder height.

These results indicate that the code functions correctly for the computation of conductivity. The residual error decreases as the radius increases; however, for small radii, the error is slightly higher than expected. This discrepancy may be associated with the definition of the boundary. Nonetheless, since the error never exceeds 10%, it is considered acceptable for the purposes of this work.

4.2. Comparison with DNS

The results obtained are also compared with the ones coming from a more reliable numerical method. To this end, a Direct Numerical Simulation (DNS) was performed on a selected patient and the outcomes are compared with those computed using **tp3d**. For what matters the process of the realization of the DNS on the geometry of the cavity, the interested reader can refer to [7].

The simulations were conducted on patient 0069, who exhibits hypertrophy of the middle and inferior turbinates in the left cavity. To execute the DNS, the geometry of the patient's internal airways was utilized, along with a sphere that simulates the external environment, providing a comprehensive model for the study.

Given that the program resolves the equations of motion for a flow in Stokes regime, in the DNS, it is decided to apply the smallest possible pressure difference, of 0.1 Pa, between the external air and the throat. This way the local Reynolds number of the flow inside the airway is maintained as low as possible. The computed results include the pressure and velocity fields. The radiodensity threshold used to extract the geometry from the computed tomography (CT) scans is set to $HU_{\text{thr}} = -300$ for both methods. To generate the mesh for the DNS it is extracted an STL file directly from the NRRD of the CT. To perform this task is used the function *threshold*, in the *segment editor* of the open source program, 3D Slicer [42]. For the purpose of ensuring the geometry extracted for the DNS and the one extracted by **tp3d** are similar, are visualized the active voxels of **tp3d** with the contour of the STL (Fig. 4.4). All the results coming from **tp3d** can be represented only to the precision of the voxels size.

The volumetric flow rates in both nostrils are computed and analyzed. It is possible to easily compare the ratio of flow rates between the two nostrils and, through slice visualizations, the pressure and velocity fields computed with both methods.

The flow rates in the CPL program are calculated as shown in Eq. (3.27). For the DNS the flow rates at a section are computed directly from the velocity field. To do this and to visualize the results from the DNS, is used the program Paraview [43]. In particular,

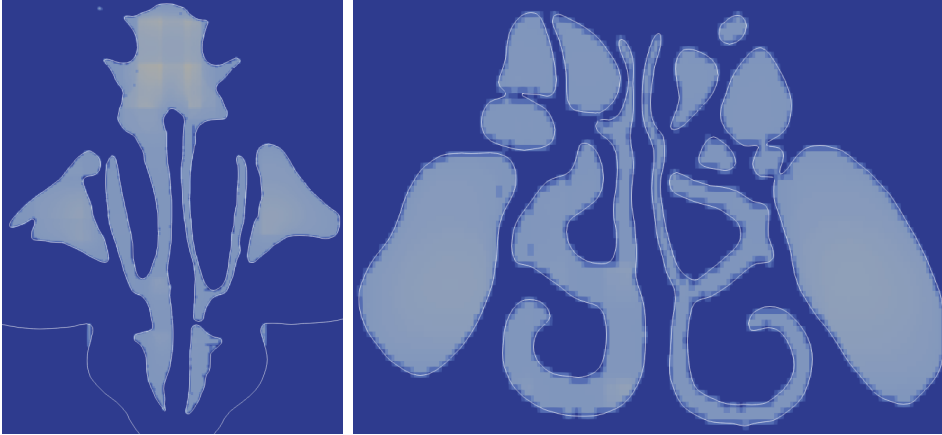


Figure 4.4: Comparison of the geometries of the STL and the one extracted with **tp3d**

Table 4.1: Flow distribution in the two nostrils.

Flow rate	tp3d	DNS
$Q_{RN}\%$	90.6%	85.3%
$Q_{LN}\%$	9.4%	14.7%

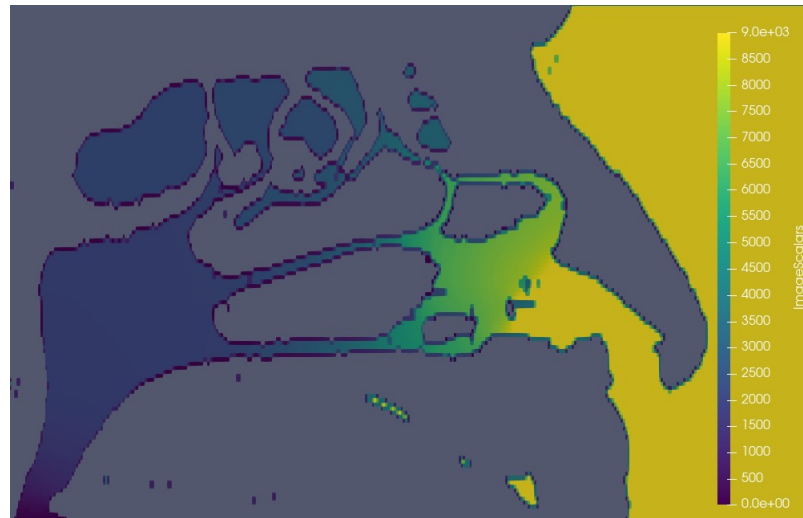
the functions used are *slice*, *clip* and *integrate variables*. The first one is used to isolate a 2D slice from the 3D geometry, the second one to take only the section of interest for the computations (e.g only one nostril, exclude external air), and the third one is needed to compute the integral in Eq. (4.6).

$$Q = \int_A \mathbf{v} \cdot \mathbf{n} \, dA \quad (4.6)$$

The results computed are reported in Table 4.1.

From the results obtained, it can be observed that **tp3d**, even if predicting the nostril through which the majority of the air enters, tends to overestimate the flow rate in the right nostril compared to the left one. The DNS solution presents a slightly more balanced distribution of flow rates.

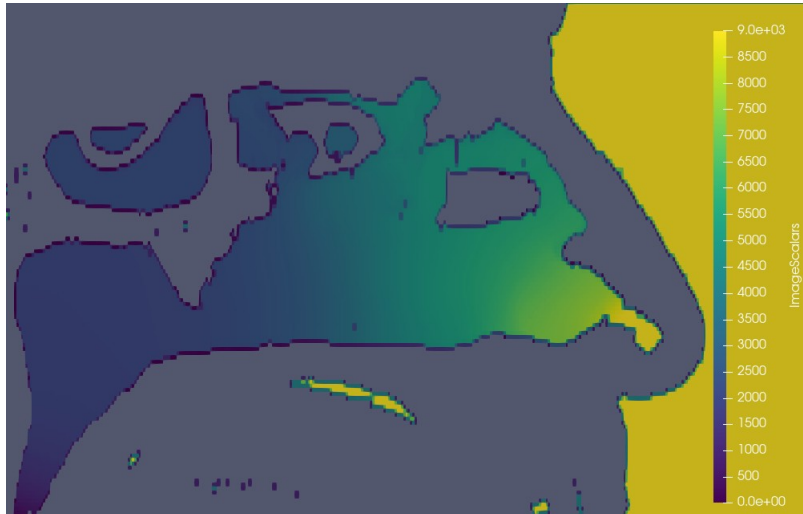
To better understand this behavior, the distributions of pressure and velocity on different slices for both solutions are compared. It is important to note that, while the figures representing results from **tp3d** are of pixel-level quality, the reconstruction used for the computations is more accurate, as described in Section 3.4. However, it is used only to compute the conductivity, so it cannot be visualized.

(a) **tp3d**

(b) DNS

Figure 4.5: Sagittal view of the pressure distribution in the left cavity

In Figs. 4.5 and 4.6, the pressure fields computed for both numerical methods are shown. It is observed that the **tp3d** code correctly characterizes the zones where the higher gradients of pressure occur. For example, this can be appreciated in the correspondence of the *meati*, in Figs. 4.5a and 4.5b, where the pressure decrease is seen in both solutions. An appreciable difference between the two is that, in the DNS solution, there is a major pressure drop when the flow starts going down the throat, which is not seen in the **tp3d** solution, where, in general, the pressure decreases more gradually along the airway. This is to be expected, because the air in the throat tends to accelerate and become more turbulent [7] and, at the same time, the air passage becomes larger. For these reasons, the description of the flow in the Stokes regime tends to deteriorate.



(a) tp3d



(b) DNS

Figure 4.6: Sagittal view of the pressure distribution in the right cavity

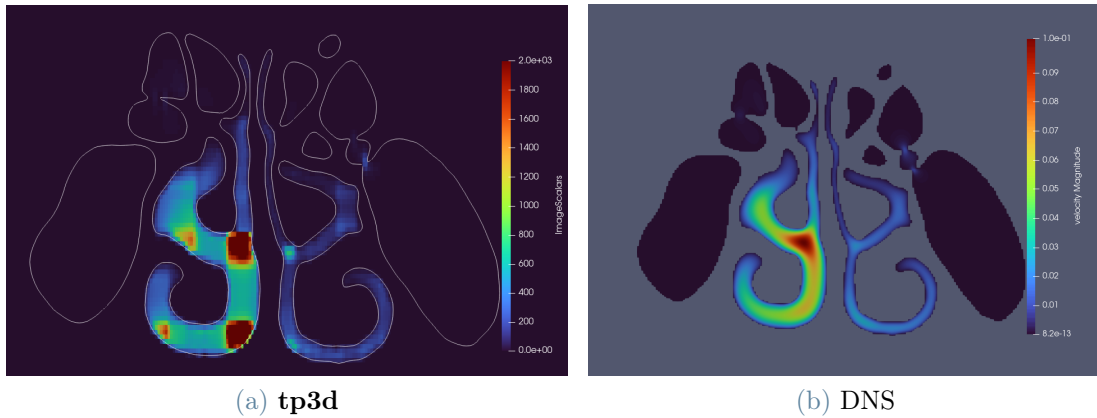


Figure 4.7: Coronal view of the velocity magnitude field

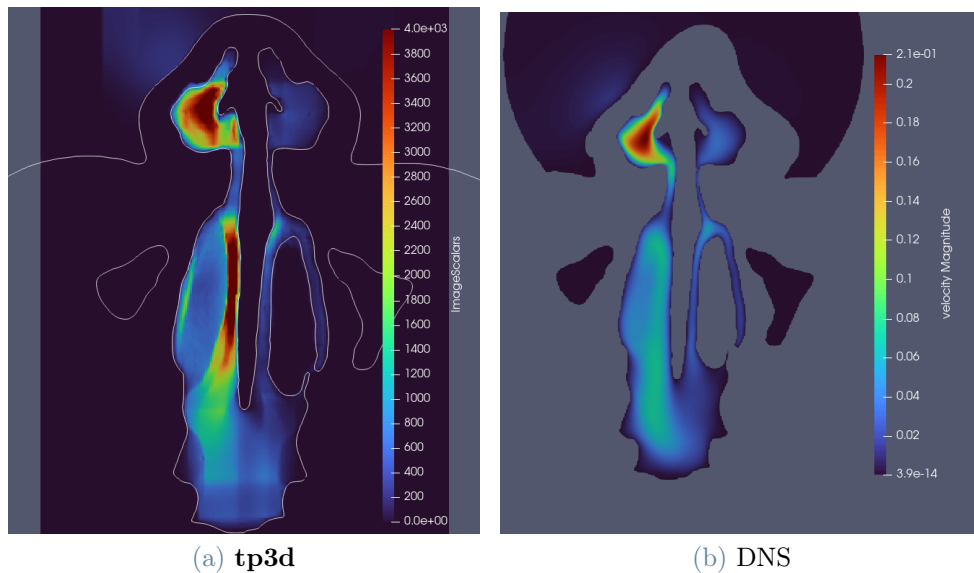


Figure 4.8: Axial view of the velocity magnitude field

In Figs. 4.7, 4.8, and 4.9, the velocity magnitude field on significant sections in all three directions is shown. It is observed that in both the **tp3d** code and the DNS solution, there is an acceleration of the flow after the nasal valve and down the throat, along with a higher velocity magnitude in the middle *meatus*. An important difference is the high velocity magnitude seen in the lower air passage for **tp3d**, visible in all the represented sections of the airway, which is absent in the DNS solution. This effect is correlated with how the permeability is computed; in fact in Fig. 4.10, representing the permeability, it is possible to recognize the same behavior. This is probably the main reason for the difference in the flow rate distribution between the **tp3d** and DNS solutions, as seen in Table 4.1.

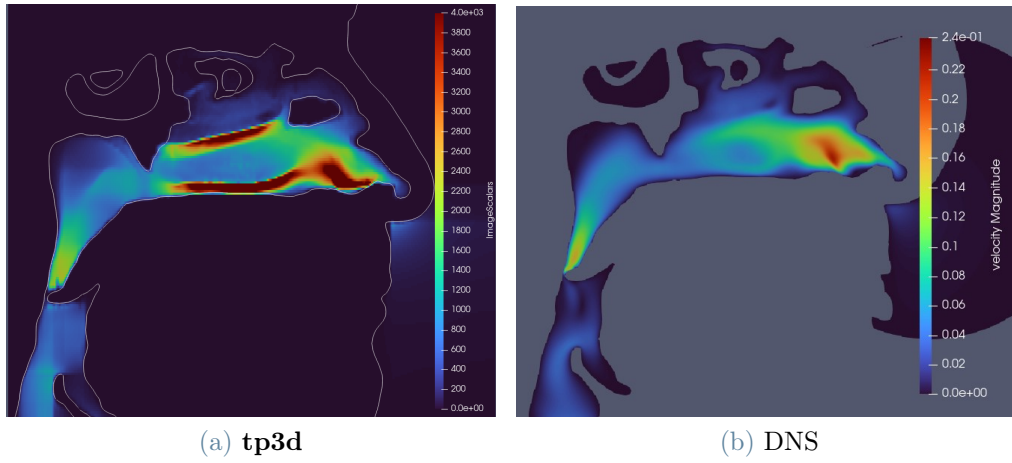


Figure 4.9: Sagittal view of the velocity magnitude field

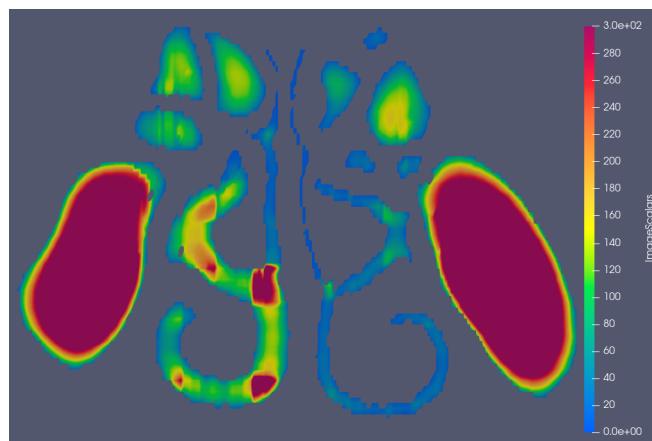


Figure 4.10: Coronal view of permeability distribution

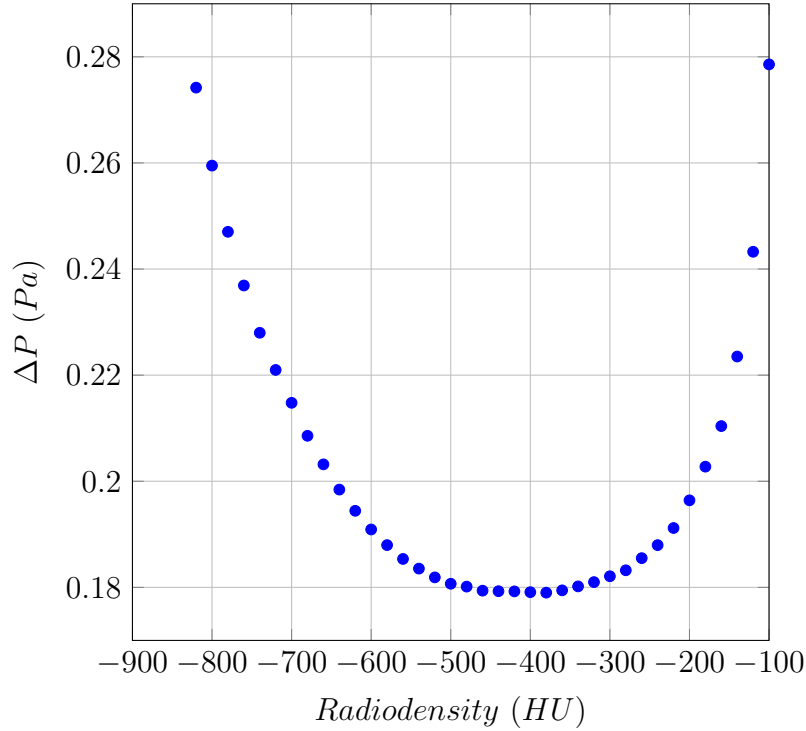


Figure 4.11: ΔP patient-0002 for different HU threshold values

4.3. A preliminary multipatient study

4.3.1. Effects of radiodensity threshold

In this section, are presented the results from simulations performed on the patients. Initially, are discussed the outcomes of simulations conducted on a single patient, imposing various radiodensity threshold values, to identify a suitable threshold to be used for the entire database. The conductivity profile considered for the computations on the database is the flat one (3.16). The patient chosen for this study is 0002, due to the fact that, for this study case, the program is able to recognize correctly the airway and perform computations across a broad range of threshold values. The results are illustrated in Fig. 4.11, where it is represented the pressure difference (ΔP) for different HU_{thr} values. A minimum ΔP is observed between -500 and -300 HU. Outside this range, the pressure difference increases for both higher and lower thresholds, for the reasons explained in section A.1.

Lower thresholds result in narrower air passages, which lead to a higher nasal resistance, as it should be. Conversely, higher thresholds introduce errors in the definition of the airway contours. This is depicted in Fig. 4.12 where it is applied a threshold $HU_{\text{thr}} = -200$, generating a geometry that has an increased nasal resistance. This effect can be attributed



Figure 4.12: Patient 0002: Geometry extracted with the correction on $HU_{thr} = -200$



Figure 4.13: Patient 0002: Geometry extracted without the correction on $HU_{thr} = -200$

to how the correction on the radiodensity value works (Section 3.4). This can be confirmed in Fig. 4.13 where the same geometry of Fig. 4.12 is extracted with the same threshold and without applying the correction, the defects on the boundary disappear.

Disabling the correction and employing a simple first-order interpolation, yields a monotonic solution curves, as shown in Fig. 4.16. For the reasons specified above, the correction should be applied only on a specific range of threshold values. To confirm that this result is not specific for a patient, it was decided to compare the results on the entire database imposing $HU_{thr} = -411$. The outcome of this study is shown in Fig. 4.15, which confirms the effect of the correction given a certain threshold has the same effect on all patients, increasing the drop of pressure and temperature.

An important observation to be made is how for more obstructed airways, the correction



Figure 4.14: Patient 0002: Geometry extracted with the correction on $HU_{thr} = -400$

has a more relevant effect. In fact, for the cases for which the drop of pressure is higher, there is a more marked difference between the results with a simple first order interpolation and the ones applying the correction to the higher order. The pressure difference and the temperature in the throat are always higher for the cases where the correction is on.

Despite this, at sufficiently low thresholds, the correction offers a more realistic model of the contour. Therefore, a radiodensity threshold around -400 HU, with the correction enabled, is the best option available (Fig. 4.14). This decision results in a smaller number of viable cases compared to using a higher threshold value, as seen in Table A.4.

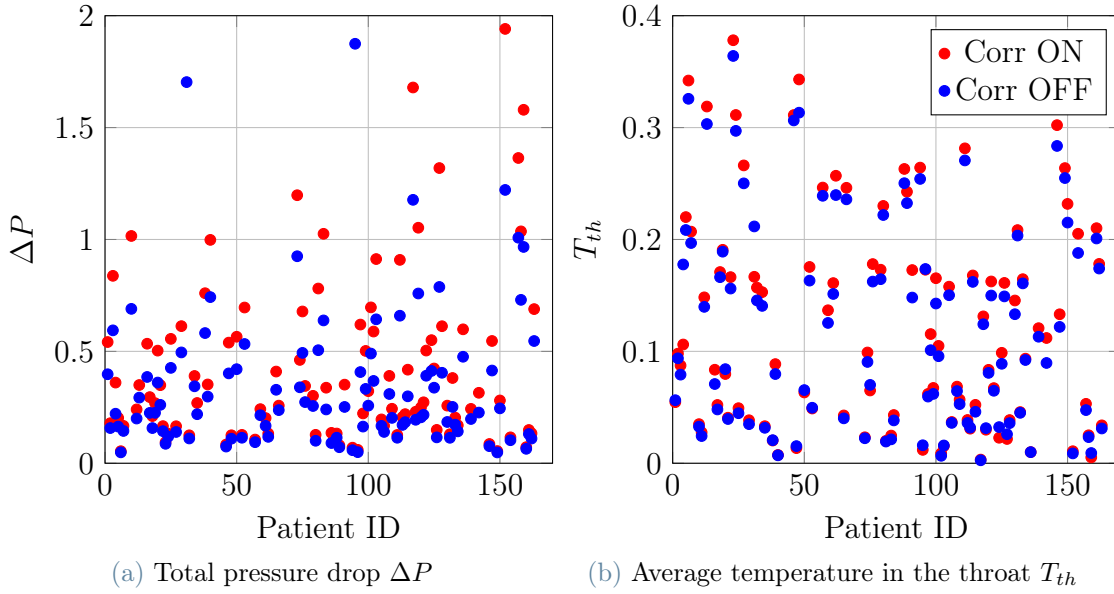


Figure 4.15: Effect of the correction on the boundary $HU_{thr} = -411$.

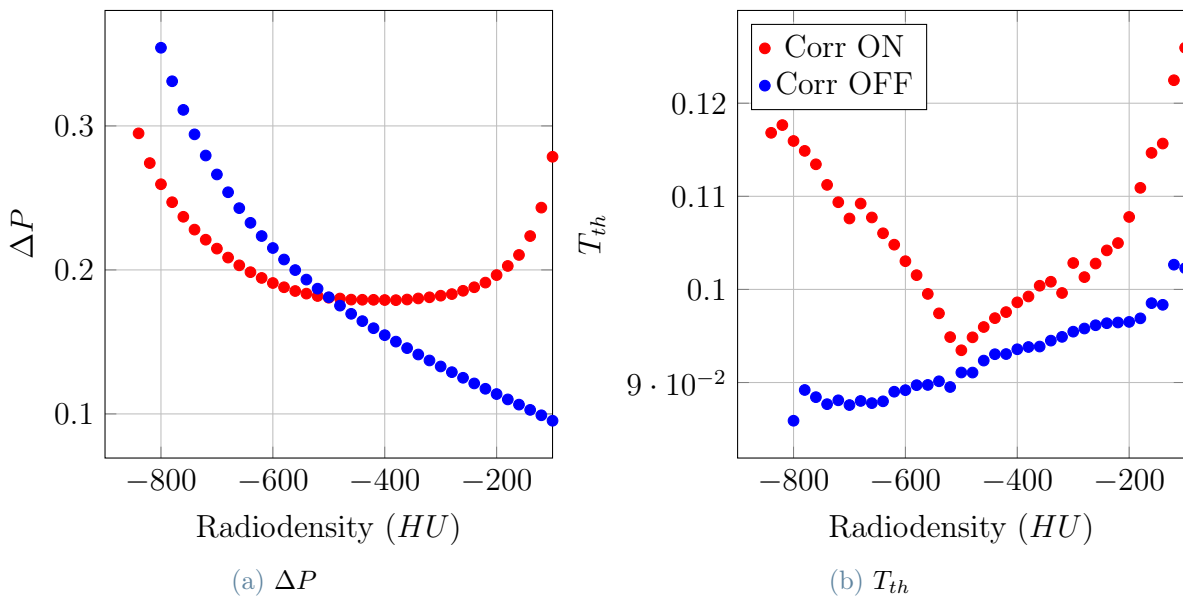


Figure 4.16: Results for patient-0002 at different HU threshold values.

4.3.2. Correlation between pathologies and results

The results presented in this section are obtained imposing a radiodensity threshold of $HU_{\text{thr}} = -411$, with 109 out of a total of 172 cases being viable for analysis. Each patient is represented by a point of a specific shape and color, indicating the type of airway pathology they have, as detailed in the legend of the plots:

- TH: Patients with turbinate pathologies (hypertrophies, paradox curvature, concha bullosa).
- SD: Patients with septal deviation or septal crest.
- TH+SD: Patients exhibiting both of the above pathologies.
- Other: Patients with other types of pathologies (e.g. polyposis).
- HEA: Patients without any identified pathology (Healthy).

A preliminary analysis of the data reveals a predominant incidence of problems affecting both the septum and turbinates. Only a few cases of healthy anatomy are observed. Given the extensive data, the findings are presented in terms of mean values in Table 4.2. When interpreting the results, it is to be considered that normally the temperature of the air inside the pharynx is higher than the external one. Values in the throat closer to zero represent a greater variation of the quantity through the airways.

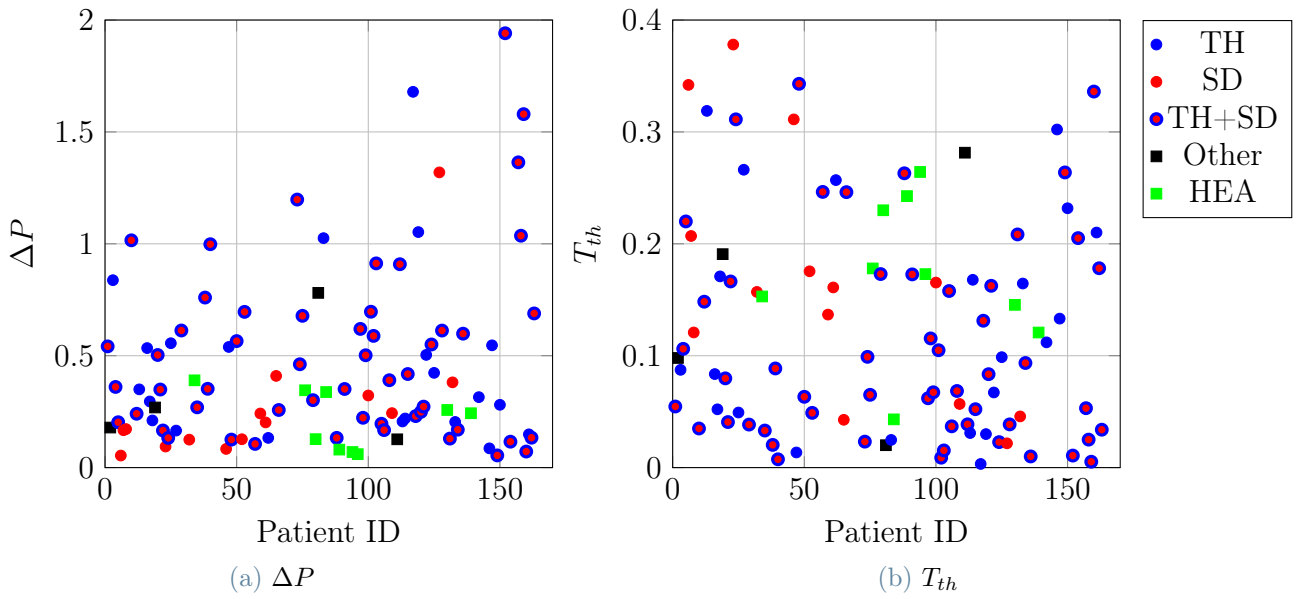
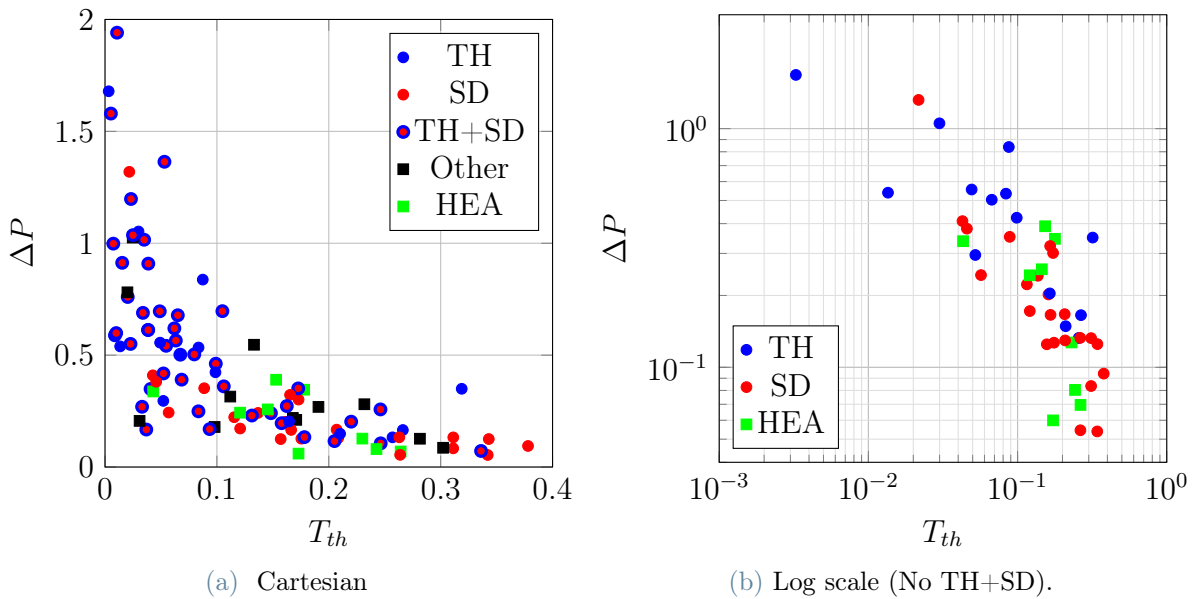
From Table 4.2 and Fig. 4.17, several general observations can be made. Patients with turbinate hypertrophies exhibit higher ΔP and lower T_{th} , while septal deviations seem to have a minimal impact on overall resistance. To convey the relationship between pressure and temperature, results are displayed as in Fig. 4.18a, demonstrating a general trend where higher pressure differences are associated with greater changes in temperature.

Patients with septal deviation and those without any pathology show a lower pressure difference compared with patients with turbinate hypertrophies. This distinction is particularly evident in Fig. 4.18b, where are excluded patients with both pathologies from the analysis and the results are represented on a logarithmic scale for clarity. The different general distribution of patients with turbinate hypertrophies and of patients without them is seen clearly by the distribution of the point in the plot.

Septal deviations do not have a strong influence on the total nasal resistance, as shown before, but are relevant on the distribution of the flow of air into the two nostrils [44]. In Fig.4.19 is represented the fraction of the total flow rate that goes into the right nostril. The points are represented with different colors on the plot based on the presence/absence and the direction of the deviation. It is clearly seen that a septal deviation to the right

Table 4.2: Mean values.

Label	Working cases	Mean ΔP	Mean T_{th}
TH	23	0.5931	0.1262
SD	14	0.2815	0.1658
TH+SD	53	0.5879	0.1066
HEA	11	0.2050	0.2184

Figure 4.17: Results at $HU_{thr} = -411$.Figure 4.18: $\Delta P - T_{th}$ plots.

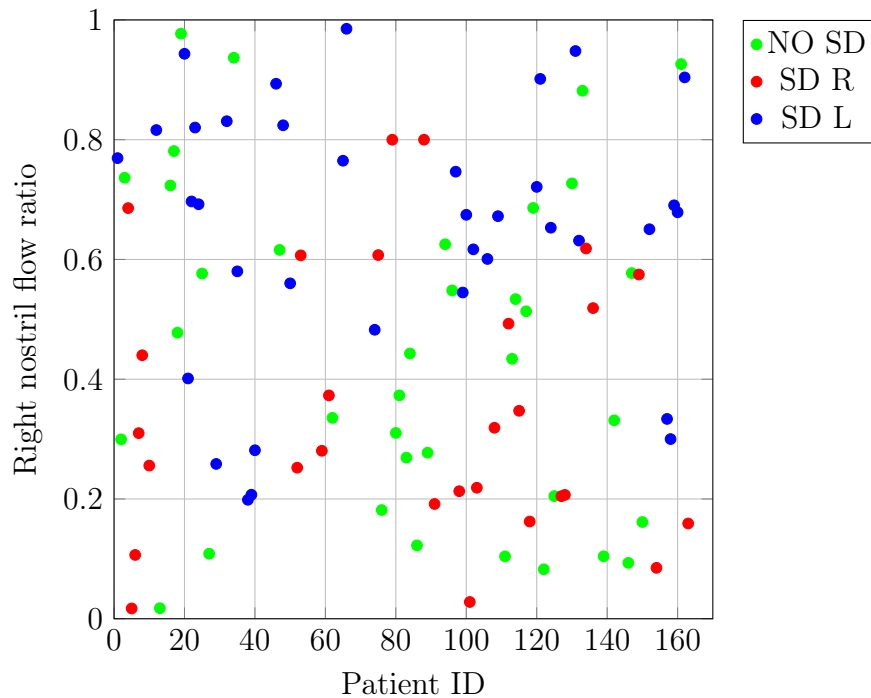
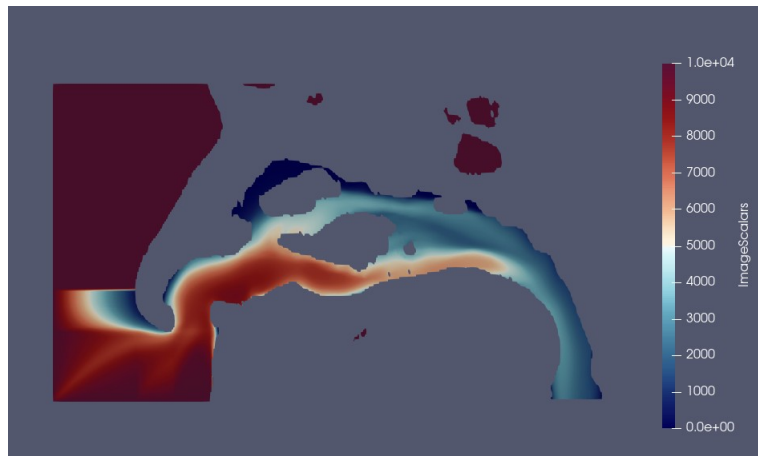


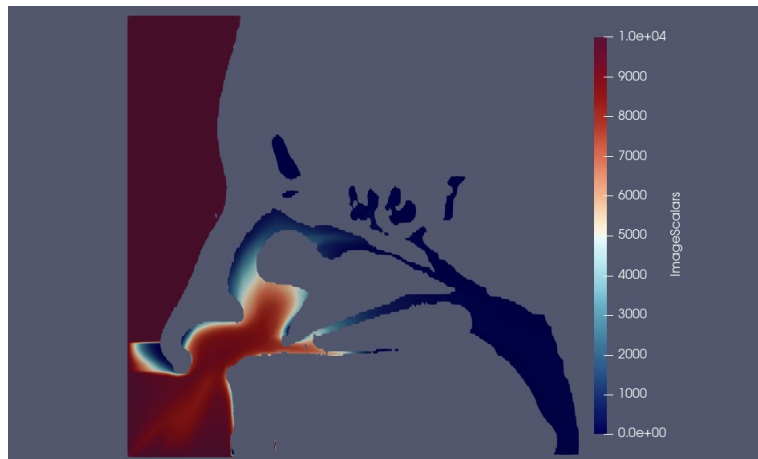
Figure 4.19: Right nostril flow Plot (Septal Deviation)

obstructs the right nostril, in fact, the mean value of air flow percentage in the right nostril for a septal deviation to the right is 35.3%, while for one towards the left is 64.5%. By logic one would get opposite results by studying the left nostril. This kind of study could not be done for turbinate hypertrophies, as it is very rare that the condition affects only one of two cavities.

To illustrate some general differences in air dynamics between healthy and obstructed nasal passages, and to show how visualizing the fields of temperature and energy dissipation computed can be useful for the interpretation of the results, two patients were selected as examples: Patient 0032 (Healthy) and Patient 0040 (Severe Turbinate Hypertrophies and Septal Deviation). Fig. 4.20 show the distribution of temperature across a sagittal slice for both patients. It is immediate to notice that in the obstructed airway the temperature changes faster and reaches a value close to the one imposed in the throat just passing through the *meati*. In the healthy patient the temperature gradient is more evenly distributed along the airway and changes faster for the flow going through the middle *meatus* than for the one in the inferior one. In Fig. 4.21 are reported the distributions of energy dissipation rate on a sagittal slice of the right air passage; for the healthy case it can be observed that the majority of the dissipation rate is in correspondence of the nasal valve before encountering the middle turbinate, while for the pathological one the dissipation is concentrated especially in the *meati*.

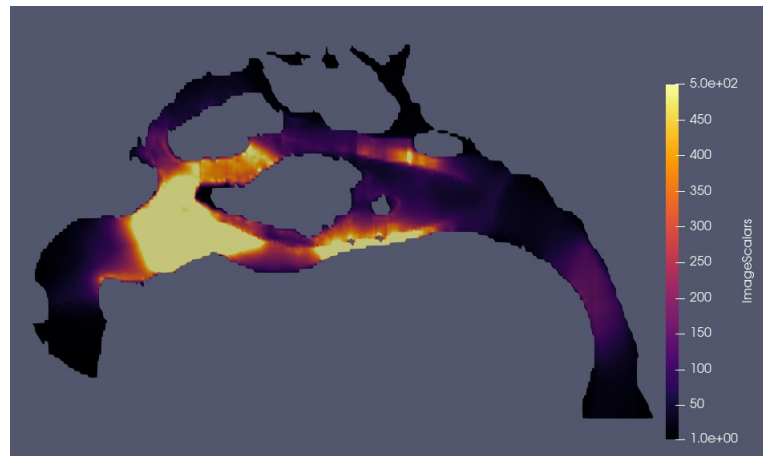


(a) Patient 0032

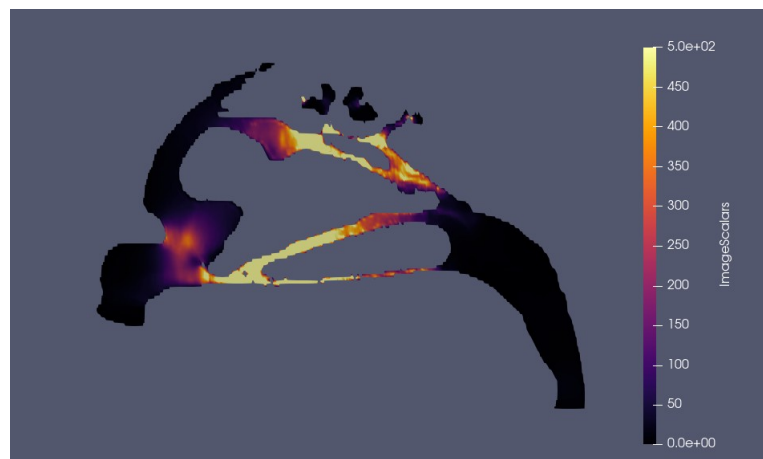


(b) Patient 0040

Figure 4.20: Sagittal view of the temperature distribution



(a) Patient 0032



(b) Patient 0040

Figure 4.21: Sagittal view of the energy dissipation distribution

5 | Conclusions

This thesis involved a preliminary approach to the code **tp3d**, including extensive work and testing, demonstrating its potential for fluid dynamics computations in a realistic nose geometry.

The initial successful test confirmed that the code functions correctly for simple geometries, demonstrating that this method can yield realistic numerical results.

The comparison with the results coming from the DNS shows that there are important differences between the two flows computed. The main problem seems to be associated with the computation of the hydraulic conductivity in **tp3d**. In fact, as observed in Fig. 4.10, there is an overestimation of the permeability computed in correspondence of some areas in the volume, that causes an overestimation of the flow of air in those zones. This phenomenon is to be studied starting from simpler geometries, such as a 90 degrees curved tube, for example.

The objective of obtaining relevant results across the entire database using the code has also been achieved. One of the most remarkable outcomes of this method is the ability to analyze a large database of diagnosed patients with minimal computational effort. In fact, for the cases that worked, the results were produced in just a few seconds per patient. The outcomes showed correlations with the medical evaluation of the patients, which is a first fundamental step for linking medical examination with the engineering approach.

The study on the effect of the radiodensity threshold to be chosen and the effect of the correction in the interpolation on the contour, gave insightful results. It was demonstrated the importance of choosing a suitable threshold for the computations and how the interpolation chosen on the boundary becomes a really important factor when considering narrow passages, as the ones in obstructed airways.

A possible improvement to be made is to make it possible for the program to work also on the problematic cases described in Section A.2. In fact, as seen, the number of scans for which **tp3d** does not give any results in output is still large.

A limitation of the code resides in the kind of flow studied, in fact the approximation to

a Stokes flow for the airflow inside the nose can be considered reliable only for extremely low inspiration rates. This has been confirmed realizing another DNS on the same patient (0069), imposing a pressure drop of 10 Pa, which is a value that should produce a normal inspiration rate at rest. The results of the two DNS are compared in Table 5.1.

Table 5.1: Comparison of the results obtained with a DNS applying different ΔP .

	$\Delta P = 10[Pa]$	$\Delta P = 0.1[Pa]$
$Q_{RN}\%$	71.6%	85.3%
$Q_{LN}\%$	28.4%	14.7%
$R[\frac{Pa \cdot s}{cm^3}]$	0.011	0.065

It is immediately apparent that the results for flow distribution and nasal resistance are not comparable. Hence it is possible to conclude that, as expected, the results coming from a flow in a low Reynolds regime inside the cavity are not valid also for other regimes. Here it is necessary to underline again that the purpose of using **tp3d**, is not to find results that are realistic for the actual behaviour of the flow inside the nose. The main objective is for it to pick up important features of the airway that may be useful to realize diagnoses and prepare surgery.

Another part of the code is being developed that includes an optimization on the geometry of the airway with an adjoint method.

6 | Bibliography

- [1] P. Illum. “Septoplasty and Compensatory Inferior Turbinate Hypertrophy: Long-Term Results after Randomized Turbinoplasty”. In: *European archives of oto-rhino-laryngology : official journal of the European Federation of Oto-Rhino-Laryngological Societies (EUFOS) : affiliated with the German Society for Oto-Rhino-Laryngology - Head and Neck Surgery* 254 Suppl 1 (1997). DOI: [10.1007/BF02439733](https://doi.org/10.1007/BF02439733) (cit. on p. 1).
- [2] P. Dinis and H. Haider. “Septoplasty: Long-Term Evaluation of Results”. In: *American journal of otolaryngology* 23.2 (2002). DOI: [10.1053/ajot.2002.30987](https://doi.org/10.1053/ajot.2002.30987) (cit. on p. 1).
- [3] J. Malik, C. Li, G. Maza, A. A. Farag, J. P. Krebs, S. McGhee, G. Zappitelli, B. Deshpande, B. A. Otto, and K. Zhao. “Computational Fluid Dynamic Analysis of Aggressive Turbinate Reductions: Is It a Culprit of Empty Nose Syndrome?” In: *International Forum of Allergy & Rhinology* 9.8 (2019), pp. 891–899. DOI: [10.1002/alr.22350](https://doi.org/10.1002/alr.22350) (cit. on pp. 1, 6).
- [4] S. Corti. “Studio numerico della fluidodinamica all’interno della cavità nasale”. MA thesis (cit. on p. 1).
- [5] C. Pesci. “OpenNOSE: an open-source procedure for the simulation of nasal aerodynamics”. MA thesis (cit. on p. 1).
- [6] L. Sufrà. “Studio comparativo di modelli di turbolenza les all’interno di una cavità nasale.” MA thesis (cit. on p. 1).
- [7] L. Vecchietti. “A direct numerical simulation code for the flow in the human nose.” MA thesis (cit. on pp. 1, 39, 41).
- [8] A. Schillaci. “Modellazione e ottimizzazione del flusso nelle cavità nasali”. MA thesis (cit. on pp. 1, 3).
- [9] R. Margheritti. “A computational geometry approach for machine learning based diagnosis of nasal breathing difficulties aided by cfd.” MA thesis (cit. on p. 1).
- [10] P. Luchini. *Introducing CPL*. Nov. 2021. arXiv: [2012.12143](https://arxiv.org/abs/2012.12143) [physics] (cit. on p. 1).

- [11] N. Mygind and R. Dahl. “Anatomy, Physiology and Function of the Nasal Cavities in Health and Disease”. In: *Advanced Drug Delivery Reviews* 29.1-2 (Jan. 1998), pp. 3–12. ISSN: 0169409X. DOI: [10.1016/S0169-409X\(97\)00058-6](https://doi.org/10.1016/S0169-409X(97)00058-6) (cit. on p. 3).
- [12] D. Doorly, D. Taylor, A. Gambaruto, R. Schroter, and N. Tolley. “Nasal Architecture: Form and Flow”. In: *Philosophical Transaction of the Royal Society* 366 (2008), pp. 3225–3246. DOI: [10.1098/rsta.2008.0083](https://doi.org/10.1098/rsta.2008.0083) (cit. on pp. 3, 7, 8).
- [13] P. Cole. “Physiology of the Nose and Paranasal Sinuses”. In: *Clinical Reviews in Allergy and Immunology* 16 (1998). DOI: [10.1007/bf02739327](https://doi.org/10.1007/bf02739327) (cit. on p. 3).
- [14] N. Jones. “The Nose and Paranasal Sinuses Physiology and Anatomy”. In: *Advanced Drug Delivery Reviews*. Nasal Vaccines 51.1 (Sept. 2001), pp. 5–19. DOI: [10.1016/S0169-409X\(01\)00172-7](https://doi.org/10.1016/S0169-409X(01)00172-7) (cit. on p. 3).
- [15] S. Zachov, P. Muigg, T. Hildebrandt, H. Doleisch, and H. Hege. “Visual Exploration of Nasal Airflow”. In: *IEEE Transaction on Visualization and Computer Graphics* 15.6 (2009), pp. 1407–1414. DOI: [10.1109/TVCG.2009.198](https://doi.org/10.1109/TVCG.2009.198) (cit. on p. 3).
- [16] *Nose, Nasal Cavities, & Paranasal Sinuses | SEER Training*. URL: <https://training.seer.cancer.gov/anatomy/respiratory/passages/nose.html> (cit. on p. 3).
- [17] *Definition of Paranasal Sinus - NCI Dictionary of Cancer Terms - NCI*. 2011. URL: <https://www.cancer.gov/publications/dictionaries/cancer-terms/def/paranasal-sinus> (cit. on p. 5).
- [18] *Ostruzioni Nasali: Concha Bullosa, Poliposi nasale, Sinusite*. URL: <https://orl.it/patologia/ostruzionenasale/> (cit. on p. 5).
- [19] G. J. M. Garcia, B. M. Hariri, R. G. Patel, and J. S. Rhee. “The Relationship between Nasal Resistance to Airflow and the Airspace Minimal Cross-Sectional Area”. In: *Journal of biomechanics* 49.9 (June 2016), pp. 1670–1678. DOI: [10.1016/j.jbiomech.2016.03.051](https://doi.org/10.1016/j.jbiomech.2016.03.051) (cit. on p. 6).
- [20] D. Demirbas, C. Cingi, H. Çakli, and E. Kaya. “Use of Rhinomanometry in Common Rhinologic Disorders”. In: *Expert Review of Medical Devices* 8.6 (Nov. 2011), pp. 769–777. DOI: [10.1586/erd.11.45](https://doi.org/10.1586/erd.11.45) (cit. on p. 7).
- [21] J. Osman, F. Großmann, K. Brosien, U. Kertzscher, L. Goubergrits, and T. Hildebrandt. “Assessment of Nasal Resistance Using Computational Fluid Dynamics”. In: *Current Directions in Biomedical Engineering* 2.1 (Sept. 1, 2016), pp. 617–621. DOI: [10.1515/cdbme-2016-0136](https://doi.org/10.1515/cdbme-2016-0136) (cit. on p. 7).
- [22] B. Üçöz. “Understanding the Mismatch between Clinical and Numerical Measurements of Nasal Resistance”. MA thesis (cit. on p. 7).
- [23] A. Lintermann and W. Schröder. “A Hierarchical Numerical Journey Through the Nasal Cavity: From Nose-Like Models to Real Anatomies”. In: *Flow, Turbulence and*

- Combustion* 102.1 (Jan. 1, 2019), pp. 89–116. DOI: [10.1007/s10494-017-9876-0](https://doi.org/10.1007/s10494-017-9876-0) (cit. on pp. 7, 8).
- [24] S. Tauwald, F. Erzinger, M. Quadrio, M. Rütten, C. Stemmer, and L. Krenkel. “Tomo-PIV in a Patient-Specific Model of Human Nasal Cavities: A Methodological Approach”. In: *Measurement Science and Technology* 35 (Feb. 2024). DOI: [10.1088/1361-6501/ad282c](https://doi.org/10.1088/1361-6501/ad282c) (cit. on p. 8).
- [25] I. Hörschler, W. Schröder, and M. Meinke. “On the Assumption of Steadiness of Nasal Cavity Flow”. In: *Biomechanics* 43 (2010), pp. 1081–1085. DOI: [10.1016/j.jbiomech.2009.12.008](https://doi.org/10.1016/j.jbiomech.2009.12.008) (cit. on p. 8).
- [26] V. Covello, C. Pipolo, A. Saibene, G. Felisati, and M. Quadrio. “Numerical Simulation of Thermal Water Delivery in the Human Nasal Cavity”. In: *Computers in Biology and Medicine* 100 (Sept. 1, 2018), pp. 62–73. DOI: [10.1016/j.combiomed.2018.06.029](https://doi.org/10.1016/j.combiomed.2018.06.029) (cit. on p. 8).
- [27] H. Calmet, K. Inthavong, H. Owen, D. Dosimont, O. Lehmkuhl, G. Houzeaux, and M. Vázquez. “Computational Modelling of Nasal Respiratory Flow”. In: *Computer Methods in Biomechanics and Biomedical Engineering* 24.4 (Mar. 12, 2021), pp. 440–458. DOI: [10.1080/10255842.2020.1833865](https://doi.org/10.1080/10255842.2020.1833865) (cit. on pp. 8, 9).
- [28] D. Tretiakow, K. Tesch, J. Meyer-Szary, K. Markiet, and A. Skorek. “Three-Dimensional Modeling and Automatic Analysis of the Human Nasal Cavity and Paranasal Sinuses Using the Computational Fluid Dynamics Method”. In: *European Archives of Oto-Rhino-Laryngology* (Oct. 17, 2020). DOI: [10.1007/s00405-020-06428-3](https://doi.org/10.1007/s00405-020-06428-3) (cit. on p. 9).
- [29] R. A. Segal, G. M. Kepler, and J. S. Kimbell. “Effects of Differences in Nasal Anatomy on Airflow Distribution: A Comparison of Four Individuals at Rest”. In: *Annals of Biomedical Engineering* 36.11 (Nov. 1, 2008), pp. 1870–1882. DOI: [10.1007/s10439-008-9556-2](https://doi.org/10.1007/s10439-008-9556-2) (cit. on p. 9).
- [30] M. Quadrio, C. Pipolo, S. Corti, F. Messina, C. Pesci, A. Saibene, S. Zampini, and G. Felisati. “Effect of CT Resolution and Radiodensity Threshold on the CFD Evaluation of Nasal Airflow”. In: *Medical & Biological Engineering & Computing* 54 (2016), pp. 411–419. DOI: [10.1007/s11517-015-1325-4](https://doi.org/10.1007/s11517-015-1325-4) (cit. on p. 10).
- [31] G. B. Cherobin, R. L. Voegels, E. M. M. S. Gebrim, and G. J. M. Garcia. “Sensitivity of Nasal Airflow Variables Computed via Computational Fluid Dynamics to the Computed Tomography Segmentation Threshold”. In: *PLOS ONE* 13.11 (Nov. 2018), e0207178. DOI: [10.1371/journal.pone.0207178](https://doi.org/10.1371/journal.pone.0207178) (cit. on p. 10).
- [32] *Teem: Nrrd: Definition of NRRD File Format*. URL: <https://teem.sourceforge.net/nrrd/format.html> (cit. on p. 10).

- [33] Y.-F. Chen, Y.-F. Liao, Y.-A. Chen, and Y.-R. Chen. “Treatment Outcome of Bimaxillary Surgery for Asymmetric Skeletal Class II Deformity”. In: *Clinical Oral Investigations* 23 (Feb. 2019). DOI: [10.1007/s00784-018-2462-6](https://doi.org/10.1007/s00784-018-2462-6) (cit. on p. 11).
- [34] W.-f. Yang, W. Choi, W.-Y. Zhu, C.-Y. Zhang, D. Li, J. Tsoi, A.-L. Tang, K.-W. Kwok, and Y.-X. Su. “Spatial Deviations of the Temporomandibular Joint after Oncological Mandibular Reconstruction”. In: *International Journal of Oral and Maxillofacial Surgery* 51 (Apr. 2021). DOI: [10.1016/j.ijom.2021.02.033](https://doi.org/10.1016/j.ijom.2021.02.033) (cit. on p. 11).
- [35] P. K. Kundu and I. M. Cohen. *Fluid Mechanics Second Edition* (cit. on p. 13).
- [36] I. Tice. *From Stokes to Darcy’s law*. URL: https://www.math.cmu.edu/~iantice/notes/stokes_to_darcy.pdf (cit. on p. 14).
- [37] C. Oltean, F. Golfier, and M. A. Buès. “Experimental and Numerical Study of the Validity of Hele–Shaw Cell as Analogue Model for Variable-Density Flow in Homogeneous Porous Media”. In: *Advances in Water Resources* 31.1 (Jan. 2008), pp. 82–95. DOI: [10.1016/j.advwatres.2007.06.007](https://doi.org/10.1016/j.advwatres.2007.06.007) (cit. on p. 22).
- [38] W. Hackbusch. “On the Multi-Grid Method Applied to Difference Equations”. In: *Computing* 20 (Dec. 1978), pp. 291–306. DOI: [10.1007/BF02252378](https://doi.org/10.1007/BF02252378) (cit. on p. 26).
- [39] S. Mittal. “A Study of Successive Over-relaxation (SOR) Method Parallelization Over Modern HPC Languages”. In: *International Journal of High Performance Computing and Networking* 7.4 (2014), pp. 292–298. DOI: [10.1504/IJHPCN.2014.062731](https://doi.org/10.1504/IJHPCN.2014.062731) (cit. on p. 26).
- [40] I. Yavneh. “On Red-Black SOR Smoothing in Multigrid”. In: *SIAM Journal on Scientific Computing* 17.1 (1996), pp. 180–192. DOI: [10.1137/0917013](https://doi.org/10.1137/0917013) (cit. on p. 26).
- [41] S. P. Sutera and R. Skalak. “The History of Poiseuille’s Law”. In: *Annual Review of Fluid Mechanics* 25. Volume 25, 1993 (Jan. 1993), pp. 1–20. DOI: [10.1146/annurev.fl.25.010193.000245](https://doi.org/10.1146/annurev.fl.25.010193.000245) (cit. on p. 35).
- [42] R. Kikinis, S. D. Pieper, and K. G. Vosburgh. “3D Slicer: A Platform for Subject-Specific Image Analysis, Visualization, and Clinical Support”. In: *Intraoperative Imaging and Image-Guided Therapy*. Ed. by F. A. Jolesz. New York, NY: Springer, 2014, pp. 277–289. ISBN: 978-1-4614-7657-3. DOI: [10.1007/978-1-4614-7657-3_19](https://doi.org/10.1007/978-1-4614-7657-3_19) (cit. on p. 39).
- [43] J. Ahrens, B. Geveci, and C. Law. “ParaView: An End-User Tool for Large Data Visualization”. In: *Visualization Handbook* (Jan. 2005) (cit. on p. 39).
- [44] T. Radulesco, L. Meister, G. Bouchet, A. Varoquaux, J. Giordano, J. Mancini, P. Dessi, P. Perrier, and J. Michel. “Correlations between Computational Fluid Dynamics and Clinical Evaluation of Nasal Airway Obstruction Due to Septal Deviation:

An Observational Study”. In: *Clinical Otolaryngology* 44.4 (2019), pp. 603–611. DOI: [10.1111/coa.13344](https://doi.org/10.1111/coa.13344) (cit. on p. 49).

- [45] P. GNU. *Free Software Foundation. Bash (3.2. 48)[Unix shell program]*. 2007 (cit. on p. 64).

A | Code execution on the database

A.1. Pathologies' labels

The labels assigned by ENT specialists are organized as shown in Table A.1. Each pathology is characterized by its severity (0 for absent, 1 for intermediate, 2 for serious) and the affected side. When the "Healthy" condition is marked as true, all pathologies are assigned a severity of zero.

Table A.1: List of all the possible labels to assign to a patient

Healthy		Septal deviation		Inf. turb. hyper.		Mid. turb. hyper.		Concha bullosa		Paradox curve	
		L	R	L	R	L	R	L	R	L	R
T	F	0/1/2	0/1/2	0/1/2	0/1/2	0/1/2	0/1/2	T/F	T/F	T/F	T/F

These labels are used to generate a binary string with “T/F” (True or False) conditions, which is automatically associated with the corresponding patient in the CSV (Comma Separated Values) file containing the results. The turbinate pathologies are collectively considered in this analysis. This decision was based on observations indicating that the presence of turbinate pathologies affects the results more significantly than the specific type or severity of each pathology, which would require more detailed analysis beyond the scope of this study.

When studying the airway comprehensively, the pathology labels are consolidated to those listed in Table A.2.

When the two passageways are studied separately, the labels are organized as in Table A.3.

Some patients have also been labeled for other pathologies, primarily nasal polyposis. Nasal polyps are benign formations resulting from chronic inflammation of the nasal and

Table A.2: Pathologies' labels used for the whole cavity

Healthy	Septal deviation	Turb. pathology
T/F	T/F	T/F

Table A.3: Pathologies' labels used for each separate airway

Healthy		Septal deviation		Turb. pathology	
		L	R	L	R
T	F	T/F	T/F	T/F	T/F

paranasal sinus mucosa. These formations can also cause airway obstruction, but they were excluded from this analysis due to the large variability of their effects on airflow through the cavity.

A.2. Procedure for the CFD simulation on all the patients

To realize the simulations on all the patients in the database in a fast and simple way, it is written an algorithm in Bash [45](Algorithm A.1) that automatizes the process by taking as inputs consecutively all the NRRD files in the database. Each patient has an associated directory with the corresponding number ID. The code loops through all the different directories and runs the program with the NRRD file associated to the ID of the patient. The results are then transcribed on a "results.csv" file, where each row corresponds to a different patient and each column to one of the quantities computed. To the csv file is added a coloumn with a string of T (true) or F (false), that identifies the pathological conditions a patient can present (Table A.2).

If **tp3d** does not produce a result for a certain patient, the code automatically generates a blank `NOTWORKING.txt` file inside the corresponding folder. Most of the time, this error occurs due to an incorrect definition of the airway, with the principal reasons being:

- Dental fillings: Often compromise the images by generating bright and dark streaking artifacts (Fig. A.1).
- Airway obstruction: Could be due to the presence of rheum or a particular condition,

Algorithm A.1 Runs **tp3d** on all the database and produces a file with the numerical results and pathologies labels for each patient

```
1: Define input directory path and program path
2: Initialize results.csv file with headers
3: for each directory in input directory do
4:   Extract directory name as patient ID
5:   if NOTWORKING.txt exists in directory then
6:     Skip the directory
7:     Continue to next directory
8:   end if
9:   if directory exists then
10:    Define path to NRRD file
11:    if NRRD file exists then
12:      Run CFD program with NRRD file
13:      Concatenate results from flowrate.txt into a single line
14:      if flowrate.txt exists then
15:        Extract residual value from log file
16:        Append results to results.csv
17:      else
18:        Log missing program output
19:        Mark directory with NOTWORKING.txt if not already marked
20:      end if
21:    else
22:      Log missing NRRD file
23:    end if
24:  else
25:    Log missing directory
26:  end if
27: end for
28: Merge labels and clean empty rows in results.csv for plotting
```

preventing the definition of the connected region of the airway (Fig. A.2).

- Image quality and cropping: This problem arises when images do not contain part of the airway due to cropping (Fig. A.3).

The program is configured to perform a maximum of 300 iterations for each case. If it does not achieve the desired residual value within this number of iterations, the final residual value is also output. Some cases were manually excluded and labeled as `NOTWORKING` because the residual remained excessively high after all iterations, making the results unreliable.

Another reason for exclusion is when the CT scan is taken with an open mouth, causing the program to compute air passing through the mouth instead of the nose, thereby providing irrelevant output for the intended purpose.



Figure A.1: Patient 0044: Effect of the teeth fillings on the CT

To study how the results change for the same patient, changing the threshold of radiodensity used to recognize solid boundaries, is created another bash loop that automatically runs the program on a set of HU values with an imposed step. In the csv file generated, together with the results, there is a column with the corresponding values of HU.

Another observed phenomenon is that increasing the threshold value tends to increase the total number of functioning cases, peaking around -250 HU, as shown in Table A.4. This occurs because some patients' nasal airways can become completely obstructed, possibly due to one of the defects mentioned earlier, which compromises the definition of the connected region. A higher threshold value allows for better topological connectivity of the airway.



Figure A.2: Patient 0058: Obstructed airway

Algorithm A.2 Iterative Computation of Flow Rates Based on HU Values

Require: Input directory with NRRD files, Program path
Initialize results file with headers
for each HU value from start value to end value with step **do**
 Calculate current HU value
 Run CFD simulation with current HU value
 Read flowrate results from generated file
 Format and append results to the results file
end for

A few cases only function with lower threshold values because sometimes the airway connects with other air-filled parts (e.g., ears, mouth), making it impossible to isolate the nasal airway. Lowering the threshold value helps keeping these passages open.

However, it is important to note that the threshold value selection will not be the sole determinant, as explained in Section 4.3.

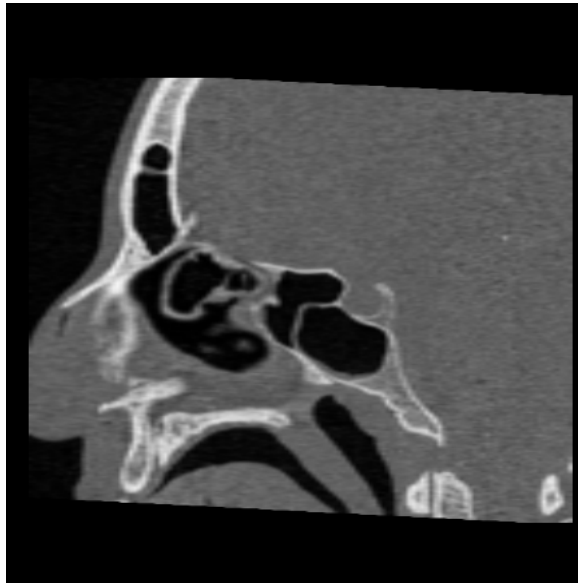


Figure A.3: Patient 0153: Cropped sagittal view

Table A.4: Functioning cases between the ones with labels.

Hu threshold values	Number of functioning cases
200	124
250	124
300	122
350	115
411	109
500	101
600	93

The scatter plots representing the results for the whole database, which will be discussed in section 4.3, are generated automatically. For their creation, various *TikZ* scripts are utilized, which take the CSV file containing the values and labels as input.

List of Figures

2.1	Nasal cavity anatomy	4
2.2	Paranasal sinuses	5
2.3	Pathological situations visualized on a coronal section of the CT	7
2.4	Reference frame and anatomical body planes.	10
3.1	Hele-Shaw configuration	16
3.2	2D representation of the patient based on depth function	18
3.3	Isolated airway	19
3.4	Bounding box and connected region	20
3.5	Computation of the position of the interface	22
3.6	Representation of the distances derived from <i>STARLINE</i> used for the computation of conductivity	24
3.7	Definite integral visualization for $a_{x_i} + dim_{x_i} < b_{x_i}$ and $a_{x_i} - dim_{x_i} > 0$. .	25
3.8	Definite integral visualization for $a_{x_i} + dim_{x_i} \geq b_{x_i}$ and $a_{x_i} - dim_{x_i} > 0$. .	25
3.9	Definite integral visualization for $a_{x_i} + dim_{x_i} < b_{x_i}$ and $a_{x_i} - dim_{x_i} \leq 0$. .	25
3.10	Definite integral visualization for $a_{x_i} + dim_{x_i} \geq b_{x_i}$ and $a_{x_i} - dim_{x_i} \leq 0$. .	26
4.1	Results for the volumetric flow rate at varius radii.	37
4.2	Velocity profile	38
4.3	Pressure variation with cylinder height.	38
4.4	Comparison of the geometries of the STL and the one extracted with tp3d	40
4.5	Sagittal view of the pressure distribution in the left cavity	41
4.6	Sagittal view of the pressure distribution in the right cavity	42
4.7	Coronal view of the velocity magnitude field	43
4.8	Axial view of the velocity magnitude field	43
4.9	Sagittal view of the velocity magnitude field	44
4.10	Coronal view of permeability distribution	44
4.11	ΔP patient-0002 for different HU threshold values	45
4.12	Patient 0002: Geometry extracted with the correction on $HU_{thr} = -200$. .	46
4.13	Patient 0002: Geometry extracted without the correction on $HU_{thr} = -200$	46

4.14	Patient 0002: Geometry extracted with the correction on $HU_{thr} = -400$. . .	47
4.15	Effect of the correction on the boundary $HU_{thr} = -411$	48
4.16	Results for patient-0002 at different HU threshold values.	48
4.17	Results at $HU_{thr} = -411$	50
4.18	$\Delta P - T_{th}$ plots.	50
4.19	Right nostril flow Plot (Septal Deviation)	51
4.20	Sagittal view of the temperature distribution	52
4.21	Sagittal view of the energy dissipation distribution	53
A.1	Patient 0044: Effect of the teeth fillings on the CT	66
A.2	Patient 0058: Obstructed airway	67
A.3	Patient 0153: Cropped sagittal view	68

List of Tables

4.1	Flow distribution in the two nostrils.	40
4.2	Mean values.	50
5.1	Comparison of the results obtained with a DNS applying different ΔP . . .	56
A.1	List of all the possible labels to assign to a patient	63
A.2	Pathologies' labels used for the whole cavity	64
A.3	Pathologies' labels used for each separate airway	64
A.4	Functioning cases between the ones with labels.	68

Acknowledgements

Desidero innanzitutto esprimere la mia gratitudine al professor Quadrio, che ha saputo suscitare il mio interesse per l'argomento e che mi ha supportato lungo tutto il percorso della tesi. Ringrazio anche il dottor Gallorini, il quale aiuto pratico è stato di grande aiuto per il lavoro.

Grazie alla mia famiglia, in particolar modo ai miei genitori e alle mie sorelle per essere stati esempio di impegno e dedizione e per tutte le opportunità che ho potuto avere grazie a loro.

Grazie a Nati per il suo amore, per la sua pazienza e per darmi la motivazione ed essere presente in tutto quello che faccio.

Grazie a tutti gli amici che, tra Lierna, Milano e Siviglia, mi hanno aiutato in questo percorso accademico. Un grazie particolare va a quelli che mi hanno accompagnato per le lunghe giornate di studio, che condividendo con me le preoccupazioni e le difficoltà hanno saputo rendere piacevoli anche i momenti più complicati.

